

# Numerical Analysis in DFT and SCAPS-1D on the Influence of Different Charge Transport Layers of $\text{CsPbBr}_3$ Perovskite Solar Cells

M. Khalid Hossain,\* Mustafa K. A. Mohammed,\* Rahul Pandey, A. A. Arnab, M. H. K. Rubel, K. M. Hossain, Md Hasan Ali, Md. Ferdous Rahman, H. Bencherif, Jaya Madan, Md. Rasidul Islam, D. P. Samajdar, and Sagar Bhattacharai



Cite This: <https://doi.org/10.1021/acs.energyfuels.3c00035>

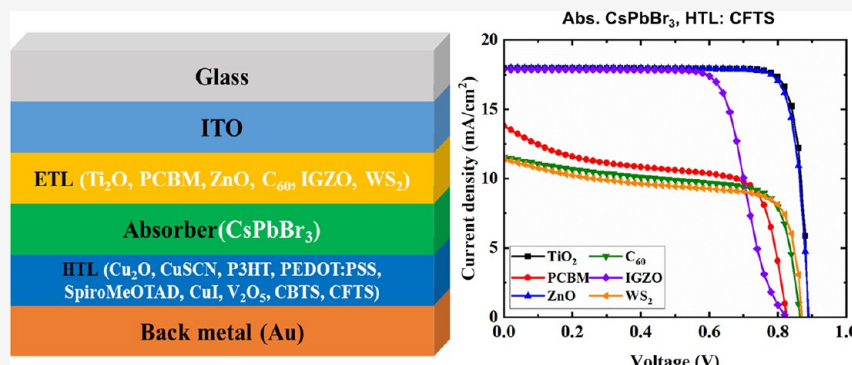


Read Online

ACCESS |

Metrics & More

Article Recommendations



**ABSTRACT:** The power conversion efficiency (PCE) of cesium lead halide ( $\text{CsPbX}_3$ , X = I, Br, and Cl)-based all-inorganic perovskite solar cells (PSCs) is still struggling to compete with conventional organic–inorganic halide perovskites. A combined material and device-related analysis is much needed to understand the working principle to explore the efficiency potential of  $\text{CsPbX}_3$ -based PSCs. Therefore, here, density functional theory (DFT) and SCAPS-1D-based studies were reported to evaluate the photovoltaic (PV) performance of  $\text{CsPbBr}_3$ -based PSCs. DFT is first applied to assess and extract structural and optoelectronic properties (band structure, density of states, Fermi surface, and absorption coefficient) of the considered absorber layer. The calculated electronic band gap ( $E_g$ ) of the  $\text{CsPbBr}_3$  absorber was 1.793 eV, which matched well with the earlier computed theoretical value. Additionally, the Pb 6p orbital contributed largely to the calculated density of states (DOS), and the electronic charge density map showed that the Pb atom acquired the majority of charges. In order to examine the optical response of  $\text{CsPbBr}_3$ , optical characteristics were computed and correlated with electronic properties for its probable photovoltaic applications. Fermi surface computation showed multiband characters. Furthermore, to look for a suitable combination of the charge transport layer, a total of nine HTLs (Cu<sub>2</sub>O, CuSCN, P3HT, PEDOT:PSS, Spiro-MeOTAD, CuI, V<sub>2</sub>O<sub>5</sub>, CBTS, and CFTS) and six ETLs (TiO<sub>2</sub>, PCBM, ZnO, C<sub>60</sub>, IGZO, and WS<sub>2</sub>) are used considering the experimental  $E_g$  (2.3 eV). The best power conversion efficiency (PCE) of 13.86% is reported for TiO<sub>2</sub> and CFTS in combination with the  $\text{CsPbBr}_3$  absorber. The effects of operating temperature, series and shunt resistances, Mott–Schottky, capacitance, generation and recombination rates, quantum efficiency, and current–voltage density were also examined. The resulting PV properties were also compared with previously published data. Results reported in this study will pave the way for the development of high-efficiency all-inorganic  $\text{CsPbBr}_3$ -based solar cells in the future.

## 1. INTRODUCTION

Recently, hybrid organic–inorganic perovskite solar cells (PSCs) have become a promising photovoltaic technology. Perovskites are composed mostly of the chemical formula  $\text{AMX}_3$ , in which A denotes a monovalent cation, M denotes metallic, and X denotes a halide anion photovoltaic (PV) candidate.<sup>1–4</sup> A cation fills the 12-fold coordinated holes in the cavity of the  $\text{MX}_6^{4-}$  octahedron, which is formed by cations and anions. These materials have advantageous optical–electrical characteristics that make them perfect for use in

photovoltaic (PV) systems, including a sufficient and tunable band gap, significant optical absorption, a long carrier diffusion length, and a high defect tolerance.<sup>5</sup> Recently, the power

Received: January 3, 2023

Revised: March 23, 2023

conversion efficiency (PCE) of PSCs reached around 25% for a small-area device ( $0.09\text{ cm}^2$ ) with a much smaller active layer than traditional commercial crystalline silicon solar cells.<sup>6</sup>

Although the PCE of the hybrid PSCs has improved quickly, their instability, such as the disintegration of perovskite material (i.e., the  $\text{CH}_3\text{NH}_3\text{PbI}_3$  device decomposes at  $85^\circ\text{C}$ ), results in a short operational life.<sup>7,8</sup> Also, heat, moisture, and UV radiation have a massive effect on the organic phase of these hybrid perovskites, causing breakdown.<sup>9</sup> An effective way to combat the instability of the PSCs is to replace the organic phase cation with an inorganic cation like  $\text{Cs}^+$ .<sup>10</sup> Many cesium lead halide perovskites have been produced that may be utilized for PSCs, including  $\text{CsPbI}_3$ ,  $\text{CsPbBr}_3$ , and  $\text{CsPbCl}_3$ , which can tolerate temperatures up to  $300^\circ\text{C}$  and have greater moisture and thermal stability than hybrid perovskites.<sup>11,12</sup>  $\text{CsPbCl}_3$  has a large band gap of over 3.0 eV, which renders it unsuitable for PSC since it will produce poor PCE. Due to the low band gap of 1.7 eV,  $\text{CsPbI}_3$  has produced a maximum PCE of  $\sim 19\%$ . These materials, despite having a narrow band gap, are not widely used because, under ambient conditions, the black  $\text{CsPbI}_3$  phase can easily degrade into a yellow phase ( $\delta\text{-CsPbI}_3$ ). As a circumstance, no such optical property for PV phenomena exists in  $\delta\text{-CsPbI}_3$ .<sup>13</sup> On the contrary,  $\text{CsPbBr}_3$  has an experimental band gap of 2.3 eV, which is more stable in terms of phase in ambient conditions in comparison with  $\text{CsPbI}_3$  and  $\text{CsPbCl}_3$ .<sup>14</sup> Moreover, the calculated band gap of  $\text{CsPbBr}_3$  perovskite using DFT methods also ranges from 1.38 to 2.66 eV<sup>15</sup> in contrast to the experimental one. As a result,  $\text{CsPbBr}_3$  PSC devices have diverse and superior light-harvesting capacities and longer-lasting stability.<sup>14</sup>

At room temperature, the structure of  $\text{CsPbBr}_3$  is orthorhombic. It has superior optical features and carrier mobility while being more stable in high temperatures and humidity.  $\text{CsPbBr}_3$  has a high defect level of tolerance and shallow transition levels. The structure deformed and changes into a tetragonal and/or cubic structure at high temperatures. At  $88^\circ\text{C}$ , it becomes tetragonal, and at  $130^\circ\text{C}$ , it shows a cubic structure. Geometric stability for  $\text{CsPbBr}_3$  is calculated using the Goldschmidt tolerance factor ( $t$ ) (eq 1).<sup>16</sup>

$$t = \frac{R_{\text{Cs}} + R_{\text{Pb}}}{\sqrt{2}(R_{\text{Cs}} + R_{\text{Br}})} \quad (1)$$

where  $R$  stands for the ionic radius,  $R_{\text{Cs}}$  denotes the ionic radii of the Cs cation,  $R_{\text{Pb}}$  denotes the ionic radii of the Pb cation, and  $R_{\text{Br}}$  denotes the ionic radii of the Br cation. The stability of the perovskite materials may be significantly impacted by the crystal structure because of variations in the lattice properties. High carrier mobility and a long diffusion length are also crucial for solar cells because they prevent carriers from recombining before electrons and holes reach the electron transport layer (ETL) and the hole transport layer (HTL), respectively, if the perovskite layer thickness exceeds the carrier diffusion length.<sup>17</sup>

Two electrodes, an ETL and an HTL, along with a perovskite absorption layer, make up the conventional PSC arrangement, which is composed of five pieces. The ETL plays a crucial function in one of them by conveying photogenerated electrons and obstructing holes. ETL and HTL both play critical roles in the PSCs' capability and reliability.  $\text{TiO}_2$ ,  $\text{SnO}_2$ , and  $\text{Nb}_2\text{O}_5$  are just a few of the materials that have been selected as the ETL in the PSCs.<sup>18,19</sup> Other examples of inorganic and organic materials that have been used as the

ETL in PSCs over time include  $\text{Al}_2\text{O}_3$ , PCBM,  $\text{C}_{60}$ ,  $\text{WO}_x$ ,  $\text{ZnO}$ ,  $\text{I}_2\text{O}_3$ ,  $\text{BaTiO}_3$ , and  $\text{PbTiO}_3$ .<sup>20,21</sup> Polymeric HTLs and inorganic or organic small molecules can be categorized into several groups depending on their chemical composition, according to established categorization methods.<sup>22</sup> Among these types of HTLs,  $\text{CuSbS}_2$ ,  $\text{NiO}$ , P3HT,  $\text{Cu}_2\text{O}$ ,  $\text{CuSCN}$ , PEDOT: PSS,  $\text{CuI}$ ,  $\text{CuO}$ ,  $\text{NiO}$ , and SpiroMeOTAD are commonly used in several studies.<sup>18–20,22</sup>

Examining a material's physical characteristics can assist us in comprehending the condition of a material system and reveal potential applications for a substance.<sup>23–28</sup> For the analysis of the optical and electronic contribution of various elements in a perovskite solar absorber material, various optical and electronic properties such as band gap and band structure, density of states (DOS), and charge density distribution are essential to explore. Nowadays, scientists use the DFT technique to conduct a theoretical investigation of the physical characteristics of relevant materials.<sup>29–32</sup> However, a few experimental and theoretical works have been found on the titled perovskite.<sup>33–35</sup> This compound was successfully prepared by López et al.<sup>33</sup> using a mechanochemical process in a  $\text{N}_2$  atmosphere, which revealed a phase transformation from orthorhombic (S.G:  $Pbnm$ , #62) to cubic (S.G:  $Pm\bar{3}m$ , #221) symmetry above room temperature. It is reported that the band gap of  $\text{CsPbBr}_3$  is possible to tune by substituting iodine in place of bromine.<sup>34</sup> It is also proved that  $\text{CsPbBr}_3$ 's band gap might be reduced and a transition from semiconducting to metallic phase could be obtained under applied pressure.<sup>34</sup> In addition, the optical properties of  $\text{CsPbBr}_3$  were thoroughly investigated, which revealed its promising candidacy for solar cell application.<sup>35</sup> Furthermore, the structural, electronic, and optical characteristics of cubic, tetragonal, and orthorhombic phases of perovskite halide  $\text{CsPbBr}_3$  are elaborately investigated using various functions to precisely understand this compound.<sup>15</sup> However, it is necessary to re-explore the structural, electronic, and optical features of the titled perovskite system using the DFT method to obtain new additional findings, which may play a significant role in device performance.

In this study, a  $\text{CsPbBr}_3$ -based perovskite-based solar cell is conducted for the very first time by considering  $\text{Cu}_2\text{O}$ ,  $\text{CuSCN}$ , P3HT, PEDOT:PSS, Spiro-MeOTAD,  $\text{CuI}$ ,  $\text{V}_2\text{O}_5$ , CBTS, and CFTS as HTLs, and  $\text{TiO}_2$ , PCBM,  $\text{ZnO}$ ,  $\text{C}_{60}$ , IGZO, and  $\text{WS}_2$  as ETLs. Using the SCAPS-1D, we thoroughly explored these ETLs and HTLs in this study to determine the ideal theoretical pairing of 54 different combinations using ITO/ETL/ $\text{CsPbBr}_3$ /HTL/Au structure for the  $\text{CsPbBr}_3$  absorber layer. Along with its structural and optical characteristics, the band gap of the selected perovskite absorber is also verified using theoretical first-principle calculations through the DFT-CASTEP framework. After determining the most potential configurations from 54 structures, we analyzed the influence of the  $\text{CsPbBr}_3$  absorber and ETLs' thickness on the PV performance, series ( $R_S$ ) and shunt ( $R_{SH}$ ) resistance, and operating temperature of the six best-performing devices. Additionally, the effects of capacitance, Mott–Schottky, recombination and generation rates,  $J$ – $V$ , and QE were assessed. Last but not the least, a comparison was made between the obtained solar cell parameters and previous studies.

**Table 1.** Input Parameters of TCO, ETLs, and Absorber Layer of this study<sup>54,55a</sup>

parameters	ITO	TiO <sub>2</sub>	PCBM	ZnO	C <sub>60</sub>	IGZO	WS <sub>2</sub>	CsPbBr <sub>3</sub>
thickness (nm)	500	30	50	50	50	30	100	800*
band gap, E <sub>g</sub> (eV)	3.5	3.2	2	3.3	1.7	3.05	1.8	2.3
electron affinity, X (eV)	4	3.9	3.9	4	3.9	4.16	3.95	3.6
dielectric permittivity (relative), ε <sub>r</sub>	9	9	3.9	9	4.2	10	13.6	6.5
CB effective density of states, N <sub>C</sub> (1/cm <sup>3</sup> )	2.2 × 10 <sup>18</sup>	2 × 10 <sup>18</sup>	2.5 × 10 <sup>21</sup>	3.7 × 10 <sup>18</sup>	8.0 × 10 <sup>19</sup>	5 × 10 <sup>18</sup>	1 × 10 <sup>18</sup>	4.94 × 10 <sup>17</sup>
VB effective density of states, N <sub>V</sub> (1/cm <sup>3</sup> )	1.8 × 10 <sup>19</sup>	1.8 × 10 <sup>19</sup>	2.5 × 10 <sup>21</sup>	1.8 × 10 <sup>19</sup>	8.0 × 10 <sup>19</sup>	5 × 10 <sup>18</sup>	2.4 × 10 <sup>19</sup>	8.47 × 10 <sup>18</sup>
electron mobility, μ <sub>n</sub> (cm <sup>2</sup> /Vs)	20	20	0.2	100	8.0 × 10 <sup>-2</sup>	15	100	4500
hole mobility, μ <sub>h</sub> (cm <sup>2</sup> /Vs)	10	10	0.2	25	3.5 × 10 <sup>-3</sup>	0.1	100	4500
shallow uniform acceptor density, N <sub>A</sub> (1/cm <sup>3</sup> )	0	0	0	0	0	0	0	0
shallow uniform donor density, N <sub>D</sub> (1/cm <sup>3</sup> )	1 × 10 <sup>21</sup>	9 × 10 <sup>16</sup>	2.93 × 10 <sup>17</sup>	1 × 10 <sup>18</sup>	1 × 10 <sup>17</sup>	1 × 10 <sup>17</sup>	1 × 10 <sup>18</sup>	1 × 10 <sup>15</sup>
defect density, N <sub>t</sub> (1/cm <sup>3</sup> )	1 × 10 <sup>15*</sup>	1 × 10 <sup>15*</sup>	1 × 10 <sup>15*</sup>	1 × 10 <sup>15*</sup>	1 × 10 <sup>15*</sup>	1 × 10 <sup>15*</sup>	1 × 10 <sup>15*</sup>	1 × 10 <sup>15*</sup>

\* In this study, these values remain constant during initial optimization to get the best combination of HTL, ETL, and back metal contact with the CsPbBr<sub>3</sub> absorber.

**Table 2.** Input Parameters of HTL in this study<sup>54a</sup>

HTL	Cu <sub>2</sub> O	CuSCN	P3HT	PEDOT: PSS	Spiro-MeOTAD	CuI	V <sub>2</sub> O <sub>5</sub>	CFTS	CBTS
thickness (nm)	50	50	50	50	200	100	100	100	100
band gap, E <sub>g</sub> (eV)	2.2	3.6	1.7	1.6	3	3.1	2.20	1.3	1.9
electron affinity, X (eV)	3.4	1.7	3.5	3.4	2.2	2.1	4.00	3.3	3.6
dielectric permittivity (relative), ε <sub>r</sub>	7.5	10	3	3	3	6.5	10.00	9	5.4
CB effective density of states, N <sub>C</sub> (1/cm <sup>3</sup> )	2 × 10 <sup>19</sup>	2.2 × 10 <sup>19</sup>	2 × 10 <sup>21</sup>	2.2 × 10 <sup>18</sup>	2.2 × 10 <sup>18</sup>	2.8 × 10 <sup>19</sup>	9.2 × 10 <sup>17</sup>	2.2 × 10 <sup>18</sup>	2.2 × 10 <sup>18</sup>
VB effective density of states, N <sub>V</sub> (1/cm <sup>3</sup> )	1 × 10 <sup>19</sup>	1.8 × 10 <sup>18</sup>	2 × 10 <sup>21</sup>	1.8 × 10 <sup>19</sup>	1.8 × 10 <sup>19</sup>	1 × 10 <sup>19</sup>	5.0 × 10 <sup>18</sup>	1.8 × 10 <sup>19</sup>	1.8 × 10 <sup>19</sup>
electron mobility, μ <sub>n</sub> (cm <sup>2</sup> /Vs)	200	100	1.8 × 10 <sup>-3</sup>	4.5 × 10 <sup>-2</sup>	2.1 × 10 <sup>-3</sup>	100	3.2 × 10 <sup>2</sup>	21.98	30
hole mobility, μ <sub>h</sub> (cm <sup>2</sup> /Vs)	8600	25	1.86 × 10 <sup>-2</sup>	4.5 × 10 <sup>-2</sup>	2.16 × 10 <sup>-3</sup>	43.9	4.0 × 10 <sup>1</sup>	21.98	10
shallow uniform acceptor density, N <sub>A</sub> (1/cm <sup>3</sup> )	1 × 10 <sup>18</sup>	1 × 10 <sup>18</sup>	1 × 10 <sup>18</sup>	1 × 10 <sup>18</sup>	1.0 × 10 <sup>18</sup>	1.0 × 10 <sup>18</sup>	1 × 10 <sup>18</sup>	1 × 10 <sup>18</sup>	1 × 10 <sup>18</sup>
shallow uniform donor density, N <sub>D</sub> (1/cm <sup>3</sup> )	0	0	0	0	0	0	0	0	0
defect density, N <sub>t</sub> (1/cm <sup>3</sup> )	1.0 × 10 <sup>15*</sup>	1 × 10 <sup>15*</sup>	1 × 10 <sup>15*</sup>	1 × 10 <sup>15*</sup>	1.0 × 10 <sup>15*</sup>	1.0 × 10 <sup>15*</sup>	1 × 10 <sup>15*</sup>	1 × 10 <sup>15*</sup>	1 × 10 <sup>15*</sup>

\* In this study, these values remain constant during initial optimization.

## 2. MATERIALS AND METHODOLOGY

**2.1. First Principal Calculations of CsPbBr<sub>3</sub> Absorber Using DFT.** In this research, the structural properties, electronic configurations, and optic response to electromagnetic radiation of CsPbBr<sub>3</sub> are examined with the use of density functional theory (DFT)-based<sup>30,36,37</sup> Cambridge Serial Total Energy Package (CASTEP).<sup>29,38</sup> Initially, the structural model of CsPbBr<sub>3</sub> is drawn by considering the formerly disclosed experimental parameters.<sup>39</sup> To obtain the ground-state structure (optimized structure), the exchange-correlation of generalized gradient approximation (GGA) is assigned in conjunction with the extensively used functional Perdew–Burke–Ernzerhof (PBE).<sup>40</sup> Pseudoatomic calculations were performed by using Cs: 5s<sup>2</sup>5p<sup>6</sup>6s<sup>1</sup>, Pb: 6s<sup>2</sup>6p<sup>2</sup>, and Br: 4s<sup>2</sup>4p<sup>5</sup> as valance electrons. Pseudopotential as core-valence states interaction and plane-wave as basis sets are chosen to perform calculations. The most popular Vanderbilt-type ultrasoft pseudopotential is treated to generate interactions between electrons and ions.<sup>41</sup> It is also essential to apply the algorithm of Broyden–Fletcher–Goldfarb–Shanno (BFGS)<sup>42</sup> during structural optimization. Although a variety of cut-off energy is used in the optimization process, 520 eV has been concluded to be compatible with it. In addition, a k-point mesh of 12 × 12 × 12 following the Monkhorst–Pack scheme<sup>43</sup> is also fitted to sample the Brillouin zone for promoting better optimization, but a comparatively higher k-point mesh of 17 × 17 × 17 is associated to exhibit the visualization of the electronic charge density map. The sampling integration is set to ultrafine quality over the first Brillouin

zone. The selected optimum converging functions of total energy, maximum ionic force, maximum ionic displacement, and maximum stress are 5 × 10<sup>-6</sup> eV/atom, 0.01 eV/Å, 5.0 × 10<sup>-4</sup> Å, and 0.02 GPa, respectively. The relaxations of atomic positions and lattice parameters are obtained after the optimization process.<sup>44</sup> The electronic and optical parameters are estimated by setting identical parameters like structural optimization. For optical properties, Eigen values and Eigen functions extracted from density functional perturbation theory (DFPT) calculations are employed in Kramers–Kronig relations.<sup>45</sup>

**2.2. SCAPS-1D Numerical Simulation.** SCAPS-1D has been used to model the perovskite-based solar cells' device properties. A good agreement between experimental findings and simulation results may be shown using SCAPS-1D.<sup>46–50</sup> These semiconductor formulas as eqs 2–4 include the Poisson equation (eq 2), which corresponds the electrostatic potential to the overall charge density, the continuity formula for holes (eq 3), and the continuity equation for electrons (eq 4), and they are employed to determine solar cell quality attributes. Furthermore, by accounting for Shockley–Read–Hall (SRH) recombination statistics, this software simulates the device's operation.<sup>51,52</sup>

$$\frac{d^2}{dx^2}\psi(x) = \frac{e}{\epsilon_0\epsilon_r}(p(x) - n(x) + N_D - N_A + \rho_p\rho_n) \quad (2)$$

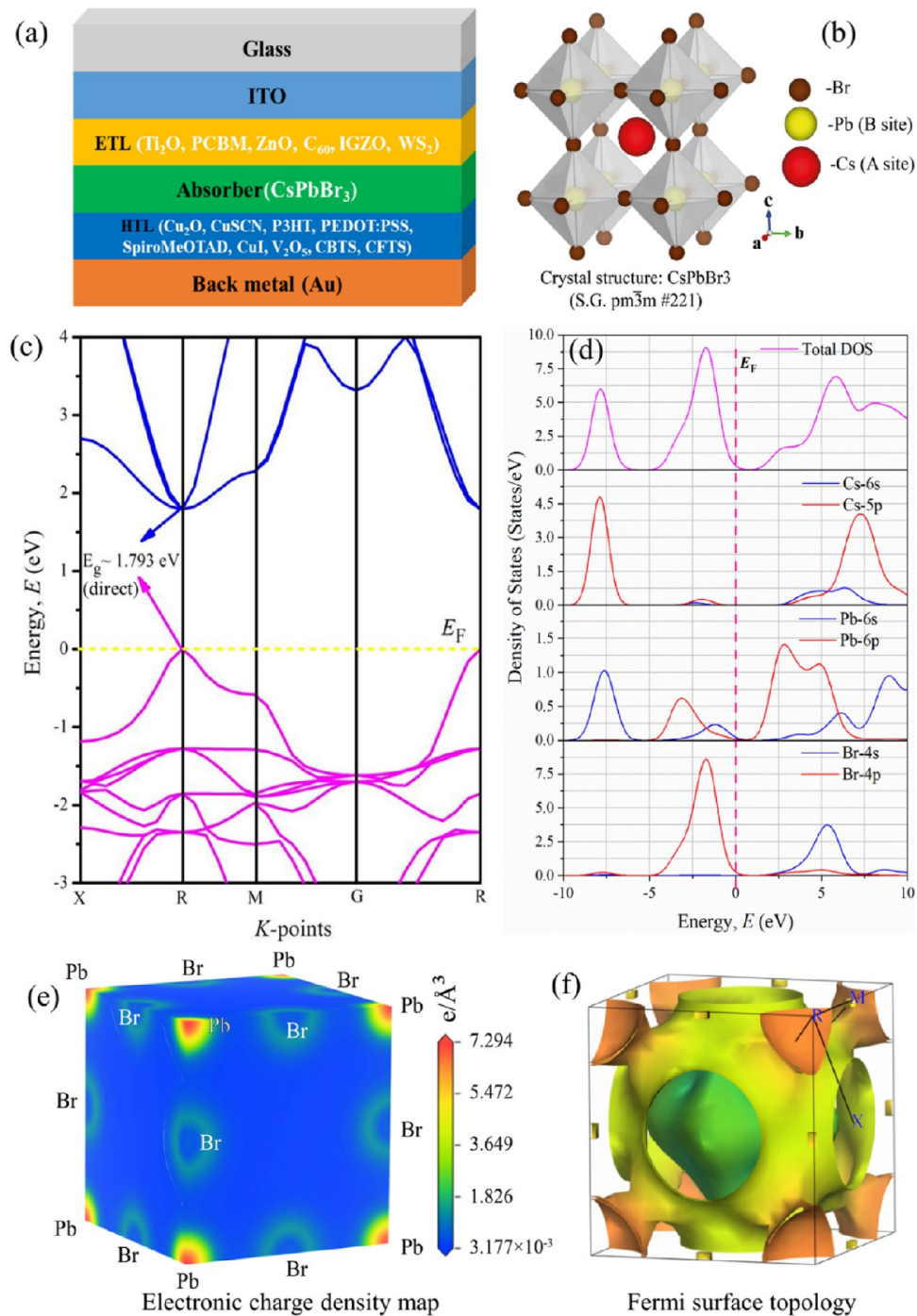


**Figure 1.** (a) Design configuration of the  $\text{CsPbBr}_3$ -based PSC, (b) crystal structure of  $\text{CsPbBr}_3$  cubic-single-perovskite semiconductor, (c) calculated band structure of  $\text{CsPbBr}_3$  along the high-symmetry direction, (d) calculated total and partial density of states of  $\text{CsPbBr}_3$ , (e) electronic charge density contour of  $\text{CsPbBr}_3$ , and (f) fermi surface topology of  $\text{CsPbBr}_3$  solar absorber material.

**Table 3. Input Parameters of Interface Defect layers<sup>54</sup>**

interface	defect type	capture cross section: electrons/holes ( $\text{cm}^2$ )	energetic distribution	reference for defect energy level	total density ( $\text{cm}^{-3}$ ) (integrated over all energies)
ETL/CsPbBr <sub>3</sub>	neutral	$1.0 \times 10^{-17}/1.0 \times 10^{-18}$	single	above the VB maximum	$1.0 \times 10^{10}$
CsPbBr <sub>3</sub> /HTL	neutral	$1.0 \times 10^{-18}/1.0 \times 10^{-19}$	single	above the VB maximum	$1.0 \times 10^{10}$

$$-\left(\frac{1}{q}\right)\frac{\partial J_p}{\partial x} - U_p + G = \frac{\partial P}{\partial t} \quad (3)$$

$$-\left(\frac{1}{q}\right)\frac{\partial J_n}{\partial x} - U_n + G = \frac{\partial n}{\partial t} \quad (4)$$

In eq 2,  $\psi$  is the electrostatic potential,  $e$  is the electrical charge,  $\epsilon_r$  and  $\epsilon_0$  are the relative and vacuum permittivities,  $p$  and  $n$  are the concentrations of holes and electrons,  $N_A$  and  $N_D$  are the charge impurities of the acceptor and donor types, and  $\rho_n$  and  $\rho_p$  are the distributions of electrons and holes, respectively. In eqs 3 and 4,  $J_n$  and  $J_p$  stand for the electron and hole current densities, respectively, and  $G$  is the generation rate. SCAPS-1D derives the steady-state response of the fundamental semiconductor equations in one dimension to resolve the abovementioned equations while considering boundary circumstances.

**2.3. CsPbBr<sub>3</sub>-Based PSC Structure.** The simulation parameters for the TCO, ETL, CsPbBr<sub>3</sub> absorber, and HTL layers are shown in Tables 1 and 2. Here, indium-doped tin oxide (ITO), 6 ETLs, CsPbBr<sub>3</sub> perovskite as an absorber, and 9 HTLs with gold (Au) as the back contact metal was chosen for the cell structure (Figure 1a). Table 3 shows the input parameters for the number of defects at the interface. The simulation was done under the circumstances of an AM1.5G simulated solar exposure to light with a power density of 1000 mW/cm<sup>2</sup> at the ambient temperature of 300 K. During the first simulation and further optimization, the traditional SCAPS model of absorption with the  $\sqrt{h\nu - E_g}$  law and experimental band gap of 2.3 eV<sup>53</sup> of the CsPbBr<sub>3</sub> absorber was utilized, as experimental data is more valuable than the theoretical one.

### 3. RESULTS AND DISCUSSION

**3.1. Analysis of DFT Results.** **3.1.1. Structural Properties of CsPbBr<sub>3</sub> Compound.** The present research considers the ideal cubic perovskite structure of CsPbBr<sub>3</sub>, which has the space group *pm̄3m* (#221). The unit cell consists of a tetrahedron that shares 6 Br atoms at face centers and is located inside the cube with a Pb atom at the body center of the cube, while the Cs atom is located at each corner of the cube (Figure 1b). The unit cell contains one molecule of five atoms of Wyckoff positions as Cs: 1b (0.5, 0.5, 0.5), Pb: 1a (0.0, 0.0, 0.0), and Br: 3d (0.0, 0.0, 0.5). The calculated structural parameters (lattice constant,  $a = 6.0115 \text{ \AA}$ , and unit cell volume,  $V = 217.24 \text{ \AA}^3$ ) of CsPbBr<sub>3</sub> exhibit a good analogy with earlier experimental values<sup>39</sup> and theoretical results.<sup>56</sup> Importantly, the negative value of formation energy ( $\Delta E_f = -3.4 \text{ eV/atom}$ ) computed via eq 5 confirms the thermodynamic stability of optimized CsPbBr<sub>3</sub>.<sup>31</sup>

$$\Delta E_f(\text{CsPbBr}_3) = \frac{[E_{\text{tot.}}(\text{CsPbBr}_3) - E_s(\text{Cs}) - E_s(\text{Pb}) - 3E_s(\text{Br})]}{N} \quad (5)$$

Here,  $E_s(\text{Cs})$ ,  $E_s(\text{Pb})$ , and  $E_s(\text{Br})$  are the energy of Cs, Pb, and Br atoms, respectively, while  $E_{\text{tot.}}(\text{CsPbBr}_3)$  is the unit cell total energy of CsPbBr<sub>3</sub>, and  $N$  represents the number of atoms in the unit cell.

**3.1.2. Band Structure and DOS of CsPbBr<sub>3</sub> Compound.** The electronic properties of a compound can provide crucial information to explain the bonding nature and related features.<sup>37</sup> These are mostly related to a material's band structure, density of states (DOS), and charge density distribution. The band structure of CsPbBr<sub>3</sub> is presented in Figure 1c. In this study, the first Brillouin zone and high symmetry  $k$ -points path X-R-M-G-R are chosen to represent band structure energies (Figure 1c). The Fermi level ( $E_F$ ) is set to zero indicated by a yellow horizontal dashed line. The perfect valence bands are pointed out by magenta lines below the  $E_F$ , while the pure conduction bands are presented by blue lines above the  $E_F$ . It is observed from Figure 1c that no band (either valence or conduction band) is crossed over the  $E_F$  without any overlapping. Therefore, it is concluded that the

compound CsPbBr<sub>3</sub> possesses an energy band gap in its band diagram. We know that computational methods usually adopt ideal or perfect stable structural symmetry of a material system and calculate relevant properties accordingly. Furthermore, the reliability of results mainly depend on the consistent lattice parameters as well as negative formation energy (eV/atom) of the calculated structure. Thus, several theoretical results might vary from experimental data.<sup>14,15</sup> The calculated band gap of 1.793 eV is somehow very close to the previous calculation,<sup>56</sup> revealing the legitimacy of the present calculation. Notably, current DFT-based simulations for the CsPbBr<sub>3</sub> band gap showed large differences from experiment data.<sup>15</sup> This discrepancy in  $E_g$  might be originated owing to the selection of calculation parameters like potentials, energy cutoff ( $E_{\text{cut}}$ ), and exchange-correlation functions during computations. However, both the conduction band minimum (CBM) and valence band maximum (VBM) is located at the R-point of the Brillouin zone, manifesting the direct semiconducting nature of CsPbBr<sub>3</sub> perovskite, which is also identical to the previous report.<sup>15,56</sup> However, the required moving energy of an electron from the valence to the conduction band of a direct band gap semiconductor is lower than an indirect band gap semiconductor. This phenomena is responsible for the better optoelectronic performance of a direct semiconducting material.<sup>57</sup> In addition, the VBM is the nearest band to the  $E_F$ , which ensures the p-type semiconducting nature of chosen perovskite.

To explain the CBM and VBM band creation, the total partial density of the states (TDOS) and partial density of the states (PDOS) of CsPbBr<sub>3</sub> are also calculated by taking GGA-PBE approximation and plotted in Figure 1d. The yellow vertical dashed line at 0 eV represents the  $E_F$ . The TDOS diagram reconfirms the existence of a band gap in the electronic structure of the studied perovskite. The valence state is mainly created due to the contribution of Pb 6s/p states with the trivial involvement of Cs 6s, Cs 5p, and Br 4s orbitals at  $E_F$ . In addition, the conduction band is also generated for major dominance of the Pb 6p orbital along with the 4s resonance of Br atoms. Specifically, the Pb 6s state is responsible for making both the VBM and CBM. As a result, in the PDOS of CsPbBr<sub>3</sub>, the Pb orbital 6s electrons are crucial for absorbing photon energy and producing photocurrent. The compound possesses p-type holes with a low value of TDOS (0.54 states/eV) at  $E_F$  according to the TDOS curve because of its semiconducting character.

**3.1.3. Electron Charge Density of CsPbBr<sub>3</sub> Compound.** A useful strategy for predicting the kind of bonds, interactions between atoms, and exchange of electrons in k-space is charge density mappings. Figure 1e shows the charge density mapping with an electron density scale along the crystal planes of (100). We notice that the Pb atom is the focal point of the charge distribution, and the charge order is uniform around this atom, which might be convenient for the photovoltaic transitions. The hybridization between both the Pb 6s/p and Br 4p orbitals, which is also evident from the DOS curve, makes the Pb–Br bond zesty. Additionally, the charge distribution map showed that the Pb and Br ions form a covalent binding<sup>54,58,59</sup> which was created as a result of the hybridization of the Pb 6s and Cs 6s states, whereas the Cs and Br ions form an ionic bond. While the ionic link strengthens the bonding nature in the functional element, the covalent character of the Pb and Br ions is utilized to form a weaker binding. However, due to the Cs atom's charge overlapping with the I-atom in the charge

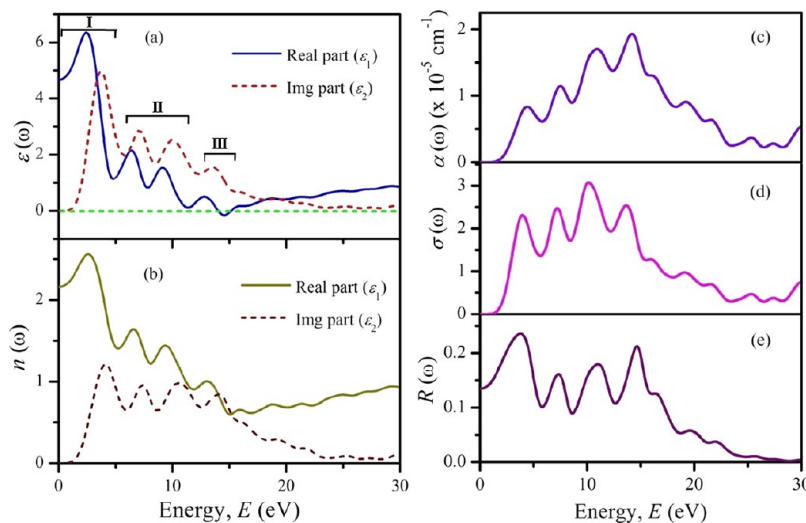


**Figure 2.** Calculated (a) dielectric function, (b) refractive index, (c) absorption, (d) conductivity, and (e) reflectivity of  $\text{CsPbBr}_3$ .

density image, it is not feasible to see it independently. According to reported perovskites<sup>29,54</sup> the charge distribution is nearly circular around all of the atoms, which is evidence of ionic bonding. The compound's ionic nature also shows metallic properties for such circular charge distribution across all of its atoms. Additionally, the electronic charge density maps along various crystal directions revealed consistent findings, which is a sign of the behavior's isotropy.

**3.1.4. Fermi Surface of  $\text{CsPbBr}_3$  Compound.** Figure 1f shows the estimated Fermi surface topology of the  $\text{CsPbBr}_3$  solar absorber at various pathways in the Brillouin zone. At the  $R(0.5,0.5,0.5)$  point of each corner, a rectangular curve shape hole sheet is connected to a massive nonuniform/deformed circular disc-like electron sheet at the  $\Gamma(0.0,0.0,0.0)$  point of origin/center. At the  $M(0.5,0.0,0.5)$  point, just above the circular necked form hole sheet, the  $\Gamma(0.0,0.0,0.0)$  point is further connected by a little plate-like hole sheet. The  $X(0.0,0.5,0.5)$  point of the body centers also contains six enormous hollow hole-like spheroid sheets that connect the  $R$ -point, where the  $R$ -point is directly connected to the center  $\Gamma(0.0,0.0,0.0)$  point in the topology of the Fermi surface. Thus, the Fermi surface contains both electron- and hole-like sheets. Interestingly, we found comparable Fermi surface topology to our recently published isostructural  $\text{CsPbI}_3$  perovskite in this report.<sup>54</sup>

**3.1.5. Optical Properties of  $\text{CsPbBr}_3$  Compound.** The response of the cubic perovskite  $\text{CsPbBr}_3$  to electromagnetic radiation is investigated by computing the refractive index, absorption coefficient, dielectric function, reflectivity, and optical conductivity. The Eigen values and Eigen functions of the perturbed system are obtained using GGA approximation. These Eigen values and Eigen functions are used to calculate the real part of the dielectric function  $\epsilon_1(\omega)$  and the imaginary part of the dielectric function  $\epsilon_2(\omega)$ . The real part of the dielectric function,  $\epsilon_1(\omega)$ , is one of the most significant optical properties. Figure 2a shows the response of the  $\epsilon_1(\omega)$  to electromagnetic radiation ranging from 0 to 30 eV. The response starts to appear at zero frequency  $\epsilon_1(0)$  at a certain point representing the dielectric constant of  $\text{CsPbBr}_3$ . It increases to reach a maximum value at energy  $\sim 2.41$  eV but reduces until it goes below zero at energy  $\sim 13.91$  eV. The dielectric constant of  $\text{CsPbBr}_3$  is 4.64. It is also shown in

Figure 2a that the first transition (region I) of  $\epsilon_2(\omega)$  occurs from the VBM to the CBM representing the critical point and corresponding to the band gap value. The response behavior can be explained in conjunction with DOS. This response makes the maximum peak because of the contribution of Pb 6s/p and Br 4p states.

On the other hand, the minor peaks in regions II and III originated due to the intraband transitions. It is also worth mentioning that both the real and imaginary parts of the dielectric function are higher at low energy regions and remarkably reduced with increasing photon energy, which is promising for a material's device performance.<sup>31</sup> The real part of the refractive index,  $n_1(\omega)$  is also plotted in Figure 2b. The behavior of the refractive index is similar to the  $\epsilon_1(0)$  except for the point where the  $n_1(0)$  starts to respond representing the actual refractive index value of this compound. The refractive index of  $\text{CsPbBr}_3$  is 2.67, which suggests the potential applications of the chosen compound in solar panels.<sup>31</sup> The refractive index increases until reaches its maximum value at an energy of  $\sim 2.62$  eV then decreases until it goes below the unity at an energy of  $\sim 11.10$  eV. This might be because the phase velocity of the light becomes greater than the speed of light itself, and this material shows the superluminality at this energy. However, the imaginary part of the refractive index,  $n_2(\omega)$  slightly exceeds the real part at  $\sim 14.08$  eV and then again falls below the real part at  $\sim 15.21$  eV. The absorption coefficient,  $\alpha(\omega)$  starts from above the zero energy, reconfirming the existence of the band gap of  $\text{CsPbBr}_3$  in its electronic structure (Figure 2c). It increases at energies in the infrared region until it gains its peak value at an energy of  $\sim 14.15$  eV. Since the  $\alpha(\omega)$  is relatively larger at low photon energy,  $\text{CsPbBr}_3$  could be potential in making solar cells. The optical conductivity,  $\sigma(\omega)$  spectrum of  $\text{CsPbBr}_3$  is demonstrated in Figure 2d. As it is proved to be a semiconducting material, the  $\sigma(\omega)$  also does not start from zero energy. It begins at  $\sim 1.65$  eV (close to the band gap value) and gives several peaks up to  $\sim 15$  eV, which finally becomes very lower with increasing energy. Figure 2c displays that the zero-energy reflectivity  $R(0)$  is  $\sim 13.6\%$  of total radiation, which is increased in the high-energy segment by the virtue of the interband carriers. Additionally, the  $R(\omega)$  displays lower values (44%) across the examined energy range, indicating significant

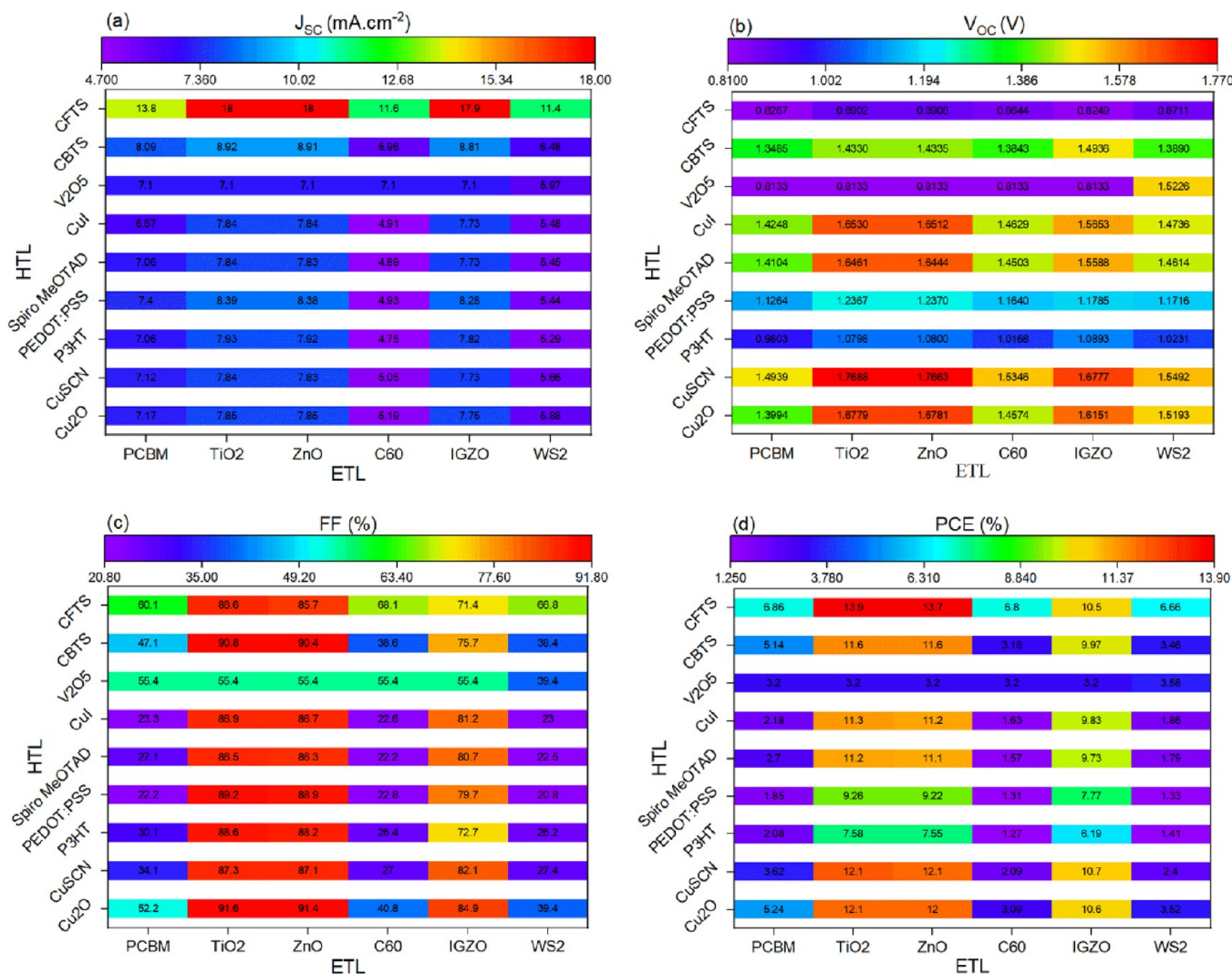


**Figure 3.** Variation of PV performance parameters of CsPbBr<sub>3</sub> absorber layer-based PSC devices for different ETLs and HTLs with Au as back metal (a)  $J_{SC}$ , (b)  $V_{OC}$ , (c) FF, and (d) PCE.

light absorptivity/transmissivity, indicating that this compound may absorb a significant amount of photons and making it appropriate for use in solar cells.<sup>31</sup>

**3.2. Analysis of SCAPS-1D Results. 3.2.1. ETL and HTL Optimization.** Mainly CsPbBr<sub>3</sub>-based PSCs with various ETL and HTL variations of different optoelectronic parameters are done because of improving the performance of the proposed cell. Figure 1a illustrates different ETLs and HTLs sandwiching the CsPbBr<sub>3</sub> absorber layer. Fifty-four (54) devices were created, and their PV performances were obtained, as shown in Figure 3a–d. PV parameters such as short-circuit current density ( $J_{SC}$ ), open-circuit voltage ( $V_{OC}$ ), fill factor (FF), and PCE are shown in Figure 3a–d, respectively. Figure 3a shows that for almost all the ETL and HTL combinations except CFTS, the  $J_{SC}$  remained below 10  $\text{mA cm}^{-2}$  and for that of CFTS, significantly improved  $J_{SC}$  is obtained. CFTS as HTL and WS<sub>2</sub>, C<sub>60</sub>, PCBM, TiO<sub>2</sub>, ZnO, and IGZO as ETL devices delivered  $J_{SC}$  values of 11.4, 11.6, 13.8, 18, 18, and 17.9  $\text{mA cm}^{-2}$ , respectively. The highest value is obtained with CFTS and TiO<sub>2</sub>, and ZnO-based HTL and ETL, respectively.  $V_{OC}$  is also obtained and depicted in Figure 3b, which showed lower  $V_{OC}$  values, i.e., below 1.1 V for P3HT, V<sub>2</sub>O<sub>5</sub>, and CFTS HTL-based devices with all the ETL; however, V<sub>2</sub>O<sub>5</sub> showed

significant elevation in  $V_{OC}$  delivering 1.5 V with WS<sub>2</sub>-based ETL.

The highest  $V_{OC}$  of 1.7 V is obtained with CuSCN HTL having TiO<sub>2</sub>, ZnO, and IGZO-based ETLs, and the performance is closely followed by Cu<sub>2</sub>O HTL-based devices having a similar set of ETLs. As shown in Figure 3c, FF showed that TiO<sub>2</sub>, ZnO, and IGZO delivered superior FF with all the HTLs except V<sub>2</sub>O<sub>5</sub>. The highest FF, close to 91%, is obtained with Cu<sub>2</sub>O HTL having TiO<sub>2</sub> and ZnO as ETL. Finally, PCE is shown in Figure 3d, which is governed by the combined effect of  $J_{SC}$ ,  $V_{OC}$ , and FF, with higher  $J_{SC}$  in the case of CFTS HTL-based devices, dominating the remaining performance parameters and showed the highest efficiency of 13.9% with TiO<sub>2</sub> based ETL. In total, 12 devices are obtained, delivering a PCE beyond 11%. A CsPbBr<sub>3</sub> perovskite absorber with CFTS, CBTS, CuI, Spiro-OMeTAD, CuSCN, and Cu<sub>2</sub>O-based HTL having TiO<sub>2</sub>- and ZnO-based ETL showed potential in delivering conversion efficiencies beyond 11%. This section concludes with 13.9% efficient PSC with architecture ITO/TiO<sub>2</sub>/CsPbBr<sub>3</sub>/CFTS/Au. In summary, CFTS shows the best performance as HTL in most cases with different ETLs; this fact is owing to its superior properties such as good conductivity that enhance the collection mechanism and the

suitable band alignment, which immunizes the device performances against the interfacial trap effect. The PV parameters of the best six solar cell structures with six different ETLs of  $\text{CsPbBr}_3$ -based PSC are listed in **Table 4**. The comparative

**Table 4.** Different Optimized Solar Cell Structures

optimized device	$V_{\text{OC}}$ (V)	$J_{\text{SC}}$ (mA/cm <sup>2</sup> )	FF (%)	PCE (%)
ITO/PCBM/CsPbBr <sub>3</sub> /CFTS/Au	0.83	13.80	60.13	6.86
ITO/TiO <sub>2</sub> /CsPbBr <sub>3</sub> /CFTS/Au	0.8902	17.98193	86.59	13.86
ITO/ZnO/CsPbBr <sub>3</sub> /CFTS/Au	0.8908	17.98002	85.66	13.72
ITO/C <sub>60</sub> /CsPbBr <sub>3</sub> /CFTS/Au	0.8644	11.55311	68.12	6.80
ITO/IGZO/CsPbBr <sub>3</sub> /CFTS/Au	0.82	17.87	71.44	10.53
ITO/WS <sub>2</sub> /CsPbBr <sub>3</sub> /CFTS/Au	0.8711	11.4333	66.84	6.66

studies on the effect of various parameters of these six structures are analyzed in the remaining part of this paper. Though CFTS is not so much used as HTL material in the literature, recently, CFTS gained attention as HTL material in perovskite solar cells<sup>60,61</sup> due to its good stability, low cost, good compatibility with a variety of perovskite materials, and high electron mobility.

**3.2.2. Band Diagram.** The energy-level alignment has a considerable impact on the PSCs' performance and efficiency. In PSCs, photogenerated electrons are introduced into the ETL conduction band while simultaneously being carried to the HTL by holes. After that, electrons and holes are gathered at the front (ITO) and rear (Au) contact metals, respectively. To extract the holes at the  $\text{CsPbBr}_3$ /HTL interface, HTL's ionization energy must be lower than that of  $\text{CsPbBr}_3$ , and ETL's electron affinity must be higher than that of the  $\text{CsPbBr}_3$  absorber. The energy band mismatch at the ETL/ $\text{CsPbBr}_3$  and  $\text{CsPbBr}_3$ /HTL interfaces also has a major influence on the device's performance metrics, including the  $J_{\text{SC}}$ ,  $V_{\text{OC}}$ , FF, and

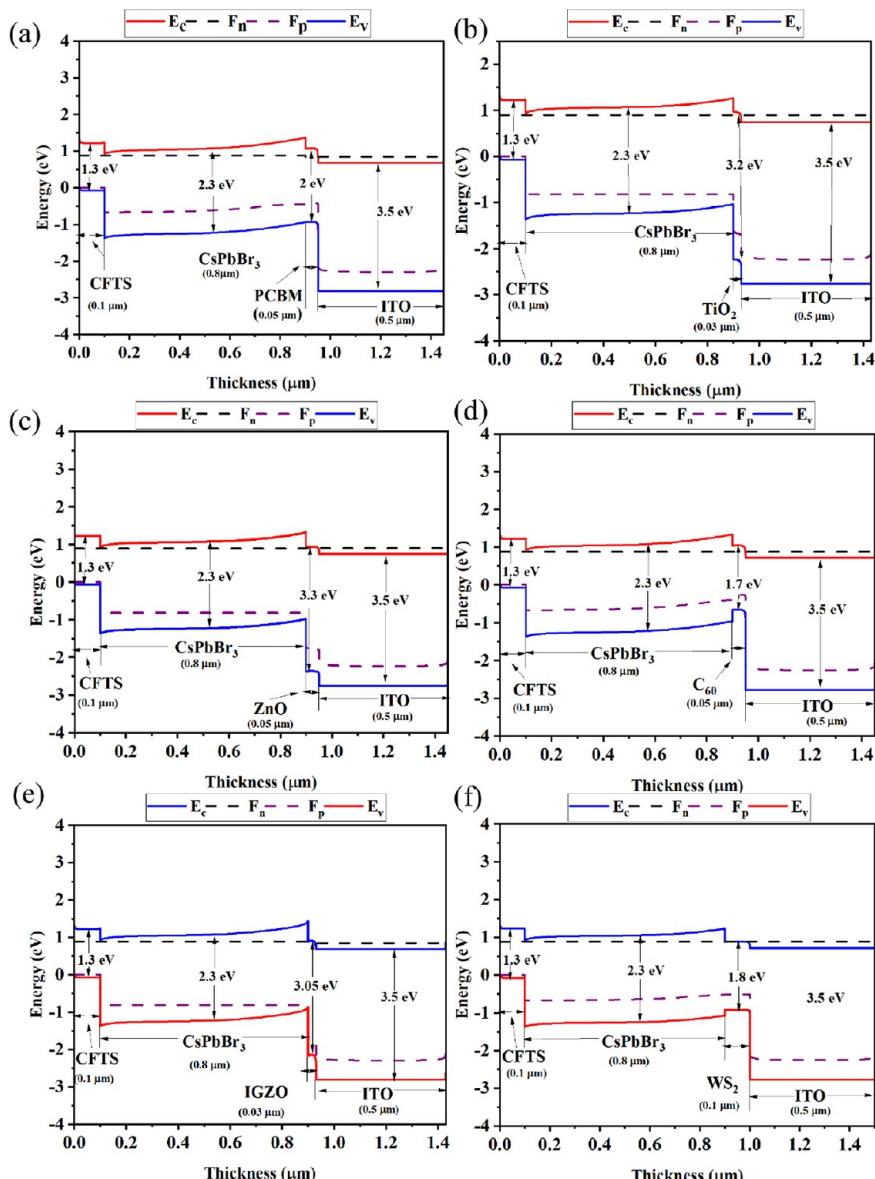


**Figure 4.** Energy band diagram of solar cells with various ETLs as (a) PCBM, (b)  $\text{TiO}_2$ , (c)  $\text{ZnO}$ , (d)  $\text{C}_{60}$ , (e) IGZO, and (f)  $\text{WS}_2$ .

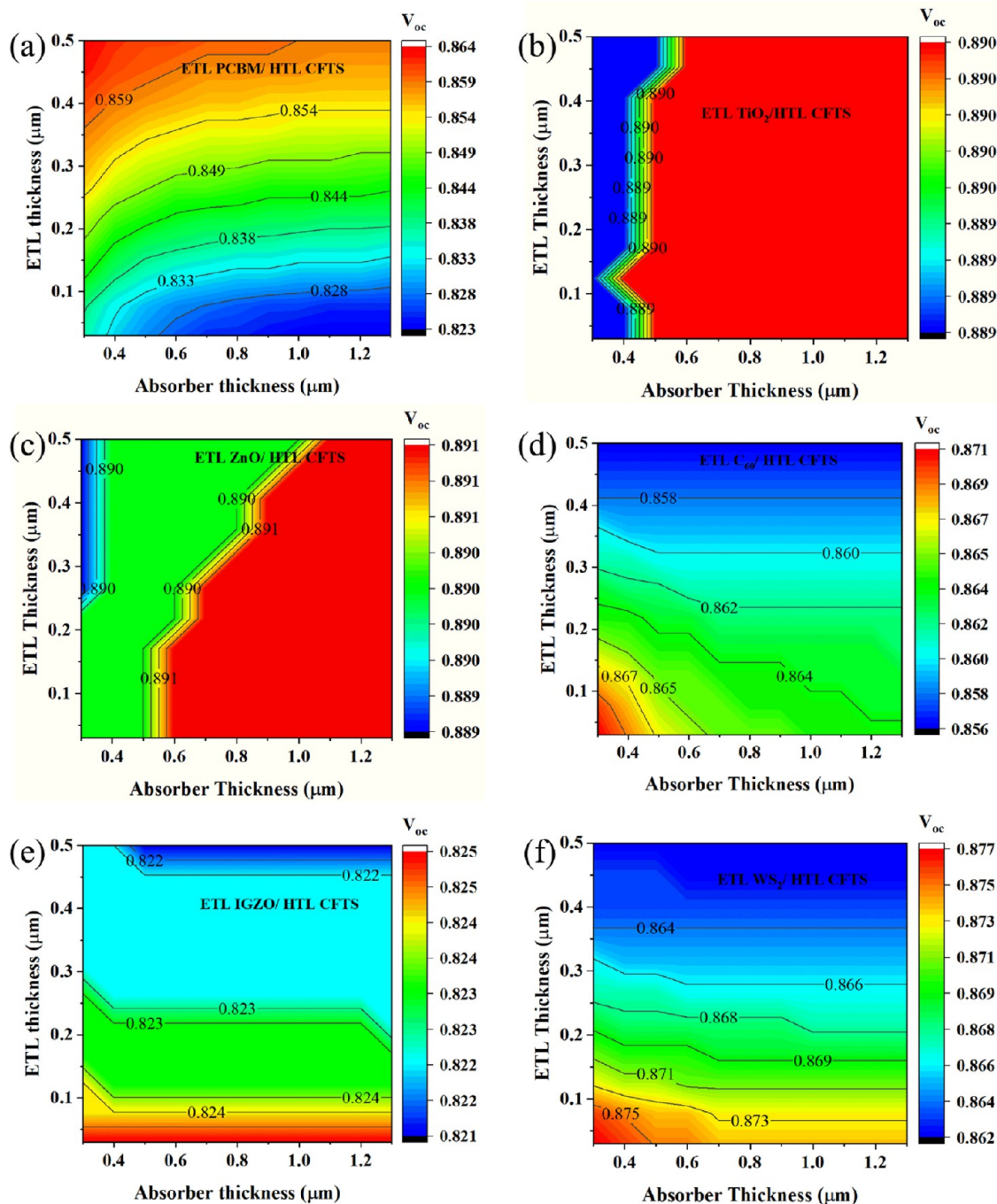


**Figure 5.** Contour mapping of  $V_{OC}$  when ETL as (a) PCBM, (b)  $TiO_2$ , (c)  $ZnO$ , (d)  $C_{60}$ , (e) IGZO, and (f)  $WS_2$ .

PCE. Figure 4 demonstrates that the fermi level is close to the conduction band and gradually enters it in both cases, but the fermi levels near the valence band are different from each other. The energy band diagram of six different solar cell architectures, including PCBM,  $TiO_2$ ,  $ZnO$ ,  $C_{60}$ , IGZO, and  $WS_2$  as ETL, is shown in Figure 4a–f.

The HTL and the absorber interface built-in potential play crucial roles in determining the  $J_{SC}$  and  $V_{OC}$  of perovskite solar cells. The HTL is responsible for transporting holes (positive charge carriers) from the perovskite layer to the conductive electrode. The quality and composition of the HTL can significantly impact the overall performance of the solar cell, including the  $J_{SC}$  and  $V_{OC}$ . A high-quality HTL can effectively reduce the recombination of holes and electrons at the

interface between the perovskite layer and the HTL, leading to an increase in the current density. In the case of the CFTS-based device, a close to fully depleted absorber layer is formed as shown in Figure 4 due to differences in the work function of the HTL and absorber. This depleted absorber layer resulted in a built-in electric field that impacted the flow of charge carriers in the solar cell. A fully depleted absorber layer results in higher  $J_{SC}$ ; however, the offset between the quasi-fermi level from the ETL/absorber and absorber/HTL is not high enough that resulted in a lower  $V_{OC}$  value.

**3.2.3. Effect of Absorber and ETL Thickness on Cell Performance.** ETL is placed between the ITO and absorber layer and can significantly affect the photon coupling in the absorber layer. Thickness analysis for the ETL is important

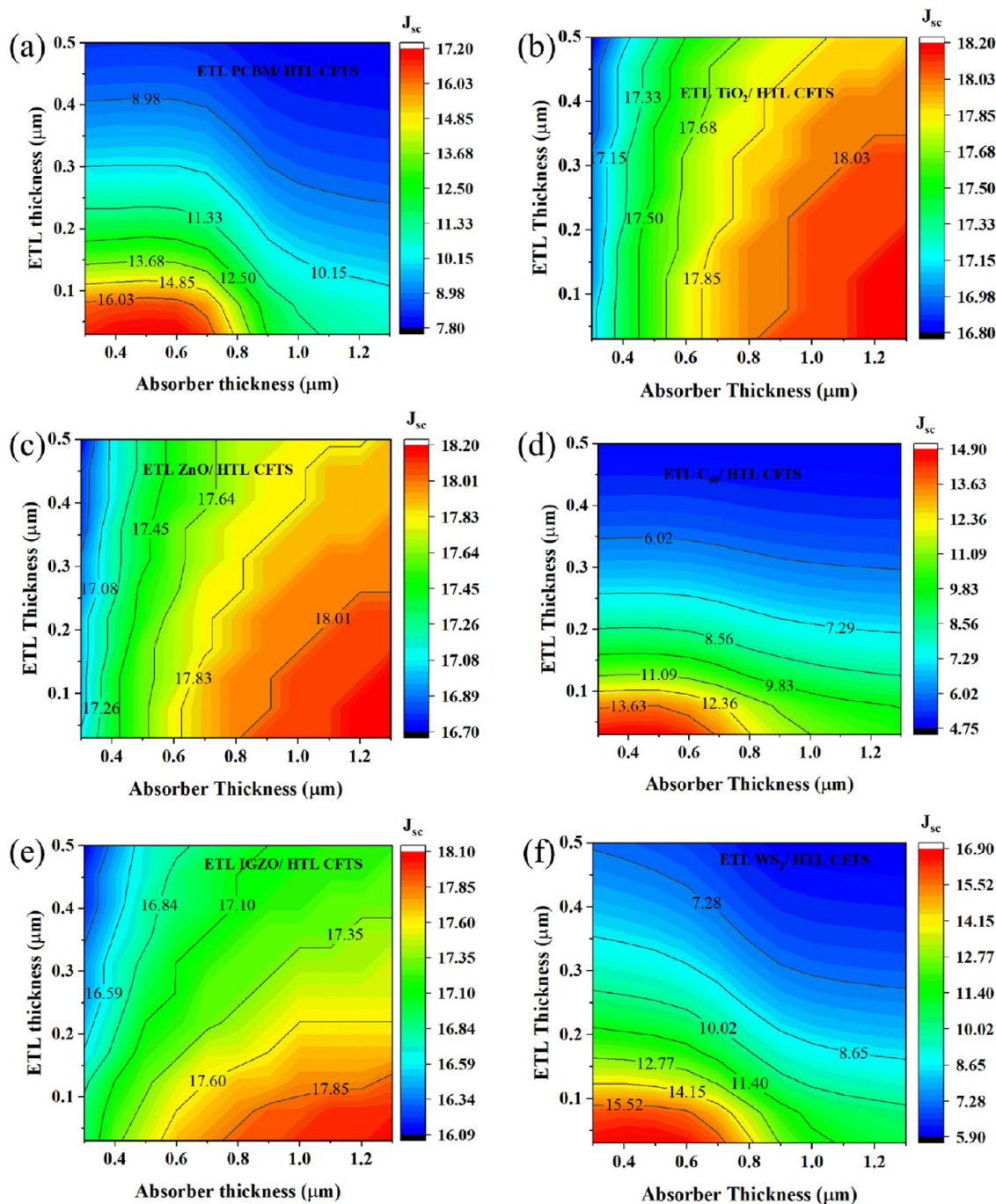


**Figure 6.** Contour mapping of  $J_{sc}$  when ETL as (a) PCBM, (b)  $\text{TiO}_2$ , (c)  $\text{ZnO}$ , (d)  $\text{C}_{60}$ , (e) IGZO, and (f)  $\text{WS}_2$ .

since it can lead to parasitic absorption in ETL and reduce the photon coupling in the absorber layer. Whereas, HTL is placed after the absorber layer and will receive photons that are transmitted by the absorber layer and hence cannot affect the optical response significantly. Therefore, here, the effect of the thickness of the  $\text{CsPbBr}_3$  absorber and PCBM,  $\text{TiO}_2$ ,  $\text{ZnO}$ ,  $\text{C}_{60}$ , IGZO, and  $\text{WS}_2$  ETLs on PSCs' performance was evaluated. Figure 5a demonstrates the  $V_{OC}$  when PCBM is used as the ETL, and CFTS are used as the HTL. The  $V_{OC}$  is around 0.864 V when the ETL thickness is greater than 0.3  $\mu\text{m}$ , and the absorber thickness has no such effect in this device. From Figure 5b,  $V_{OC}$  increased to 0.891 V and was unchanged at  $\geq 0.5 \mu\text{m}$  absorber thickness, and in this case,  $\text{TiO}_2$  ETL had no such effect on the configuration. However,

Figure 5c shows that both the absorber and ETL thickness have an impact on  $V_{OC}$ ; in this instance, the absorber thickness was  $\geq 0.6 \mu\text{m}$ , resulting in a  $V_{OC}$  of 0.890 V, where  $\text{ZnO}$  is used as ETL and CFTS is considered as HTL. Figure 5d shows that neither the thickness of the absorber nor the ETL had a substantial impact on  $V_{OC}$  (0.871 V) when  $\text{C}_{60}$  was the ETL and CFTS was the HTL-associated solar cell structure. According to Figure 5e, where IGZO serves as the ETL and CFTS serve as the HTL, we can see that a low ETL thickness is the primary cause of a high  $V_{OC}$  of 0.825 V, which was among the lowest of all devices. Finally, Figure 5f shows that neither the absorber nor ETL thickness has significantly affected  $V_{OC}$  (0.877 V) when  $\text{WS}_2$  is taken as ETL and CFTS is employed as HTL.

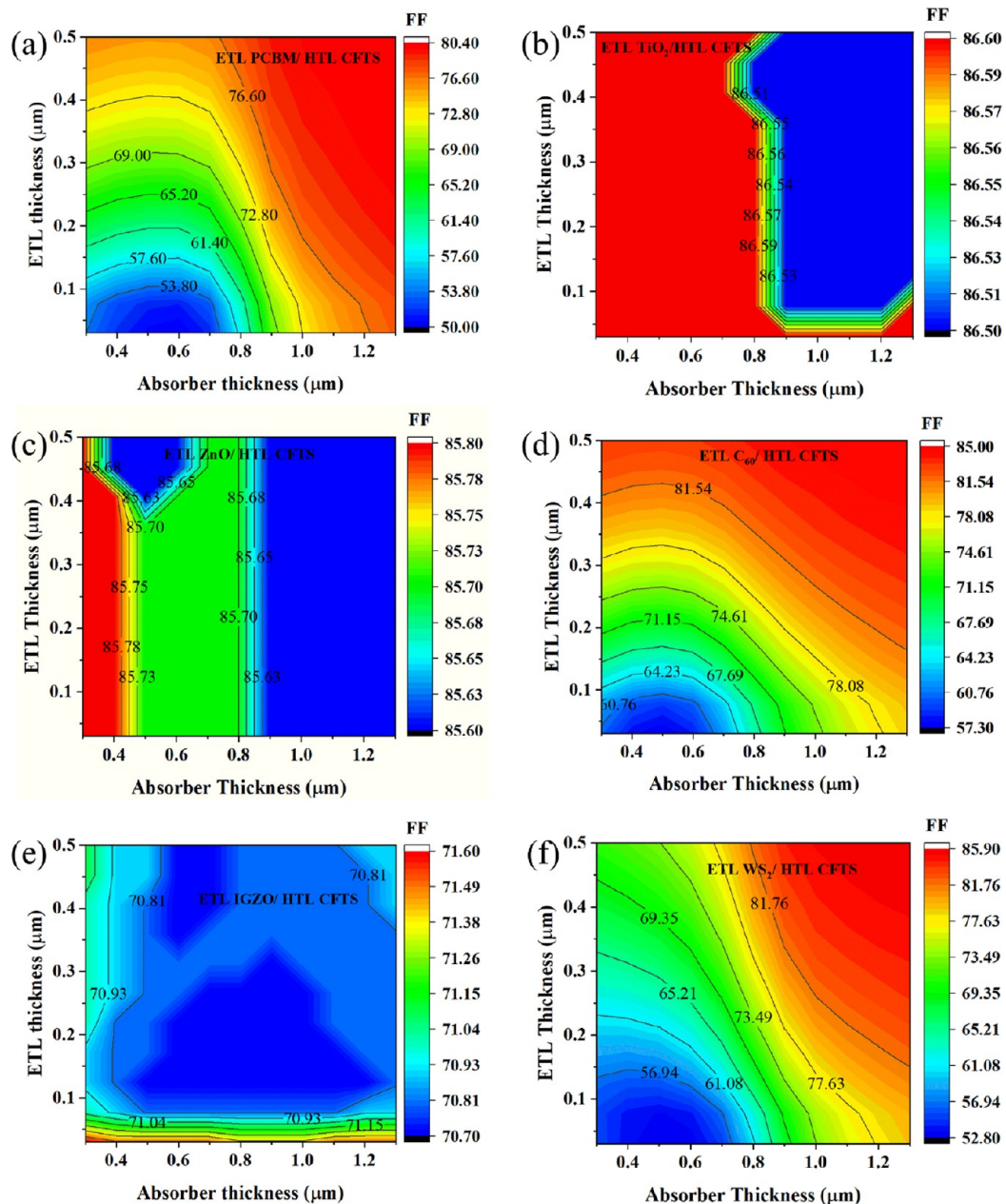


**Figure 7.** Contour mapping of FF when ETL as (a) PCBM, (b)  $\text{TiO}_2$ , (c)  $\text{ZnO}$ , (d)  $\text{C}_{60}$ , (e) IGZO, and (f)  $\text{WS}_2$ .

The case of the  $J_{\text{SC}}$  variation after varying the absorber and ETL thickness simultaneously is illustrated in Figure 6. Figure 6a indicates the case of PCBM as an ETL and CFTS as an HTL. In that case, the value of  $J_{\text{SC}}$  was higher at  $17.20 \text{ mA/cm}^2$ , when the absorber and ETL thicknesses were  $\leq 0.7$  and  $< 0.1 \mu\text{m}$ , respectively. In the case of  $\text{TiO}_2$  as ETL and CFTS as the HTL-associated solar cell, it shows a  $J_{\text{SC}}$  of  $18.20 \text{ mA/cm}^2$ , when the ETL and absorber thicknesses were taken at a range of 0.03 to  $0.3 \mu\text{m}$  and 0.8 to  $1.3 \mu\text{m}$  according to Figure 6b. However, in the case of  $\text{ZnO}$  as ETL and CFTS as the HTL-associated solar cell structure, it showed a  $J_{\text{SC}}$  of  $18.2 \text{ mA/cm}^2$  when the absorber thickness was  $\geq 1.1 \mu\text{m}$  and ETL thickness was  $\leq 0.1 \mu\text{m}$  according to Figure 6c. When  $\text{C}_{60}$  as ETL and CFTS as HTL is used, the associated solar cell structure shows a higher range ( $14.9 \text{ mA/cm}^2$ ) of  $J_{\text{SC}}$ , when both the absorber and ETL thickness is lower, i.e., in between 0.3 and  $0.5 \mu\text{m}$  and 0.03 and  $0.05 \mu\text{m}$ , respectively (Figure 6d). When IGZO as

ETL and CFTS is taken as the HTL-associated PSC structure, it shows a  $J_{\text{SC}}$  of  $18 \text{ mA/cm}^2$ , when the absorber thickness is set from 0.8 to  $1.3 \mu\text{m}$  and ETL thickness is 0.03 to  $0.1 \mu\text{m}$  according to Figure 6e. Finally,  $\text{WS}_2$  as ETL and CFTS as HTL-associated PSC structure show a higher  $J_{\text{SC}}$  of  $16.9 \text{ mA/cm}^2$ , when both absorber and ETL thicknesses were lower, i.e., in between 0.3 and  $0.6 \mu\text{m}$  and 0.03 and  $0.05 \mu\text{m}$ , respectively (Figure 6f).

Figure 7 shows the changing nature of FF for variation of the absorber and ETL thickness for PSCs. According to Figure 7a, it was observed that when PCBM was taken as ETL and CFTS as HTL, then PSC showed 80.40% FF when ETL and absorber thicknesses were taken from 0.3 to  $0.5 \mu\text{m}$  and 1.1 to  $1.3 \mu\text{m}$ . However,  $\text{TiO}_2$  as an ETL-associated solar cell structure shows 86.60% FF when the absorber thickness is  $< 0.8 \mu\text{m}$  according to Figure 7b. The ETL  $\text{ZnO}$  and HTL CFTS-associated PSC structure showed 85.80% FF when the absorber thickness was

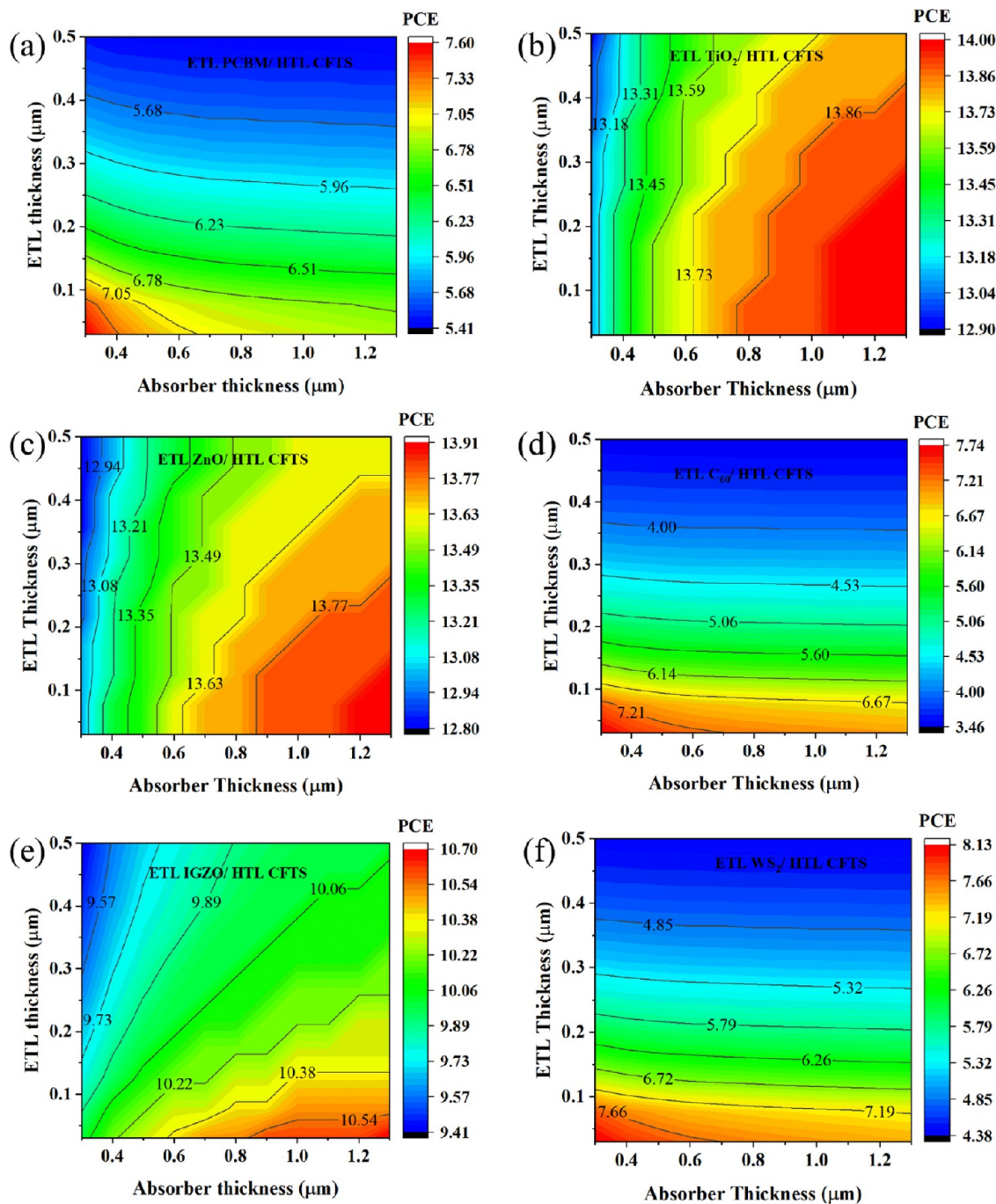
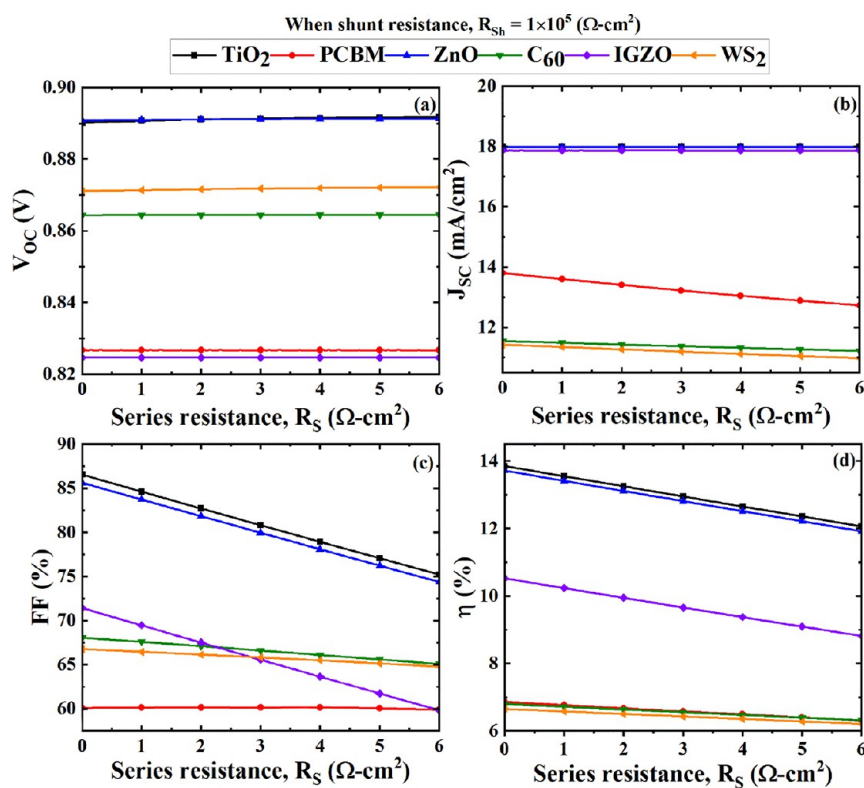


**Figure 8.** Contour mapping of PCE when ETL as (a) PCBM, (b) TiO<sub>2</sub>, (c) ZnO, (d) C<sub>60</sub>, (e) IGZO, and (f) WS<sub>2</sub>.

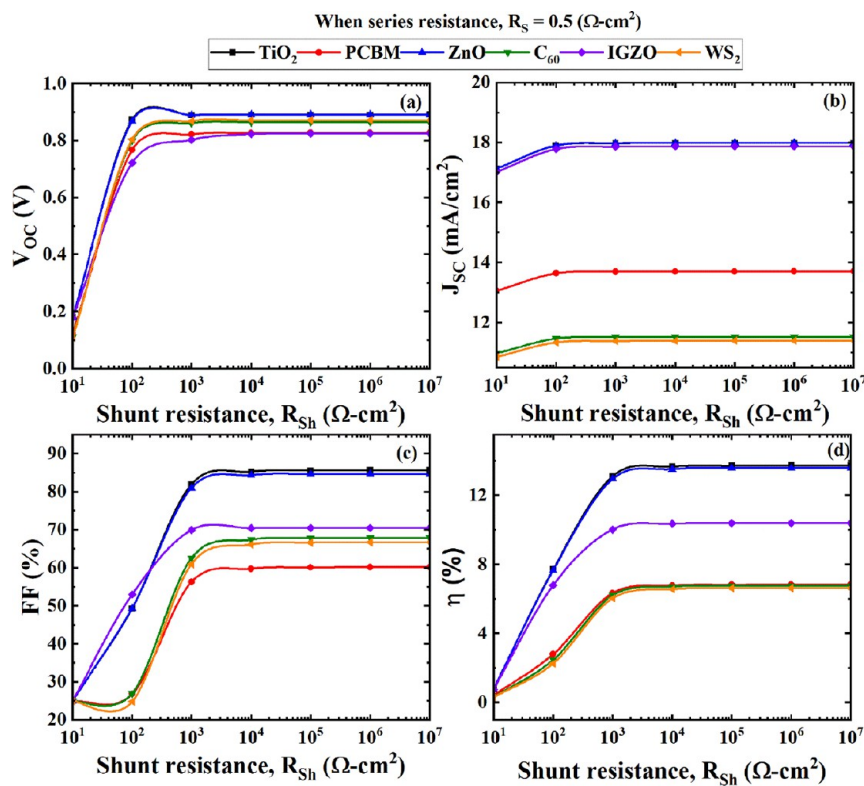
<0.5 μm according to Figure 7c. From Figure 7d, we observed that when C<sub>60</sub> was taken as ETL and CFTS as HTL, then the PSC showed almost an FF of 85% when ETL and absorber thicknesses were >0.40 and >0.80 μm, respectively. However, according to Figure 7e, we observed that when IGZO was taken as ETL and CFTS was taken as HTL, PSC showed 71.60% FF when ETL thicknesses were <0.05 μm. Finally, when WS<sub>2</sub> was taken as ETL and CFTS was taken as HTL, then the PSC structure showed >80% FF at ETL and absorber thicknesses of >1 and >0.3 μm, respectively, according to Figure 7f.

Figure 8 shows the effect on PCE of the varying absorber and ETL thickness simultaneously for six studied PSCs. According to Figure 8a, it was seen that when PCBM is taken

as ETL and CFTS as HTL-associated PSC, it showed almost 7.6% PCE when absorber and ETL thicknesses were 0.4 and 0.05 μm, respectively. In Figure 8b, TiO<sub>2</sub> was taken as ETL and CFTS as HTL; it showed almost 14% PCE when the absorber thickness was taken at a range of 0.8 to 1.3 μm and ETL thickness was taken at a range of 0.03 to 0.4 μm. In Figure 8c, ZnO was taken as ETL and this structure shows almost the same nature as Figure 8b. However, according to Figure 8d where C<sub>60</sub> is taken as ETL, this structure showed almost 7.74% PCE when both ETL and absorber thicknesses were taken as lower, i.e., 0.3 to 0.4 μm and 0.03 to 0.05 μm, respectively. When IGZO was taken as ETL, then the structure showing 10.70% PCE after taking the absorber thickness higher (>1 μm) and ETL thickness lower (<0.05 μm) according to Figure



**Figure 9.** Effect of series resistance on  $\text{CsPbBr}_3$  perovskite solar cells' (a)  $V_{OC}$ , (b)  $J_{SC}$ , (c) FF, and (d) PCE.



**Figure 10.** Effect of shunt resistance on  $\text{CsPbBr}_3$  perovskite solar cells' (a)  $V_{OC}$ , (b)  $J_{SC}$ , (c) FF, and (d) PCE.

8e. Finally, when  $WS_2$  was taken as ETL, then the PSC structure showed almost 8.13% PCE by taking the both absorber and ETL thickness lower, i.e., almost 0.3 and 0.03  $\mu\text{m}$ , respectively.

**3.2.4. Effect of Series Resistance.** In this section, the performance parameters of  $\text{CsPbBr}_3$  absorber-based solar cells were observed for  $R_S$ , while  $R_S$  was varied from 0 to  $6 \Omega\cdot\text{cm}^2$ . According to Figure 9, efficiency is slightly decreased with the

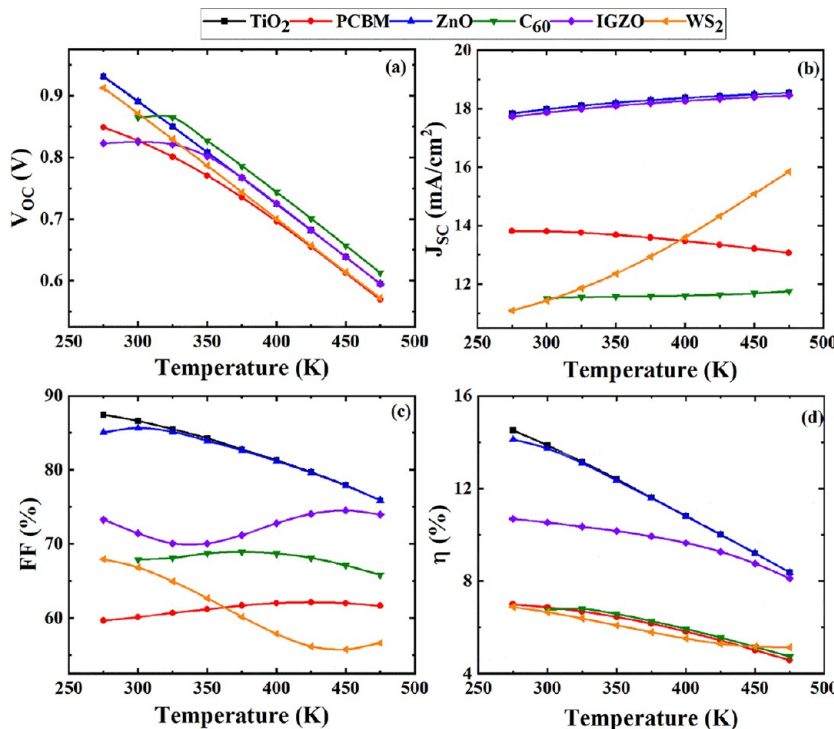


**Figure 11.** Effect of different temperatures on  $CsPbBr_3$  perovskite solar cells' (a)  $V_{OC}$ , (b)  $J_{SC}$ , (c) FF, and (d) PCE.

increase of  $R_S$ . Therefore, the loss of efficiency, particularly the FF, in large-area PSCs and modules is the combined effect of several variables, including uniformity,  $R_S$ , and  $R_{Sh}$ .<sup>62–65</sup> In PSCs, the sources of  $R_S$  include electrode resistance, interface contact resistance, and semiconductor resistance. Andriessen and colleagues discovered that, when the active zones were accelerated, electrodes with higher series resistance resulted in a bigger loss of PSC efficiency.<sup>66</sup> Figure 9a shows that  $V_{OC}$  was almost constant in the case of all the six solar cell structures for increasing the  $R_S$ , but PCBM ETL exceptionally showed a  $V_{OC}$  of almost <0.83 V, which was higher than the IGZO as ETL-associated structure structures. An almost similar  $J_{SC}$  was observed according to Figure 9b when  $\text{TiO}_2$ , ZnO, and IGZO ETL-based structures showed a higher  $J_{SC}$ , which was almost 18  $\text{mA}/\text{cm}^2$ . However,  $C_{60}$ , PCBM, and  $WS_2$  as ETL-based structures showed a  $J_{SC}$  of <14  $\text{mA}/\text{cm}^2$ , which was much lower than  $\text{TiO}_2$ , ZnO, and IGZO ETL-associated structures, and PCBM ETL-associated structures showed a very low  $J_{SC}$  of 13  $\text{mA}/\text{cm}^2$  but greater  $J_{SC}$  than  $WS_2$  and  $C_{60}$  as an ETL-associated structure. Also, Figure 9c shows decreasing FF with respect to  $R_S$ , in which  $\text{TiO}_2$  and ZnO as ETL-associated solar cells show almost 87% FF initially and  $R_S$  was decreased at about <85% FF. In order to PCBM,  $C_{60}$ , IGZO, and  $WS_2$  as ETL connected mode respective solar cells showed the lowest FF than  $\text{TiO}_2$  and ZnO ETL connected mode which started from almost 60%, 68%, 72%, and 67%, respectively. According to Figure 9d,  $\text{TiO}_2$  and ZnO as ETL-associated structures showed initially almost 14% PCE but it reduces after increasing the  $R_S$ ; a similar pattern was observed in the case of PCBM,  $C_{60}$ , IGZO, and  $WS_2$  ETL-associated structures, but these structures show lower PCE than the  $\text{TiO}_2$  and ZnO ETL structures.

**3.2.5. Effect of Shunt Resistance.** Internal resistances in PSCs are caused by light-absorbing materials, interface barriers, charge-collecting interlayers, and metal-based electrodes.<sup>67</sup>

The Shockley equation, represented by eqs 6 and 7, explained the expected behavior of a solar cell's  $J-V$  characteristic under ideal one-sun illumination conditions.<sup>68</sup>

$$J_{SC} = J_{PH} - J_o \left[ \exp\left(\frac{q_e(V - JR_S)}{nkT_e}\right) - 1 \right] - \frac{V - JR_S}{R_{Sh}} \quad (6)$$

$$V_{OC} = \left( \frac{nkT_e}{q_e} \right) \ln \left\{ \frac{J_{PH}}{J_o} \left( 1 - \frac{V_{OC}}{J_{PH} R_{Sh}} \right) \right\} \quad (7)$$

where  $q_e$  is the elementary charge,  $J_{PH}$  is the photocurrent density,  $J_o$  is the reverse bias saturation current density,  $R_S$  is the series resistance,  $R_{Sh}$  is the shunt resistance,  $n$  is the diode ideality factor,  $k$  is the Boltzmann constant ( $1.38 \times 10^{23} \text{ J K}^{-1}$ ), and  $T_e$  is the ambient temperature (298 K).

The effect of  $V_{OC}$ ,  $J_{SC}$ , FF, and PCE values with  $R_{Sh}$  variation is visually represented in Figure 10, where  $R_{Sh}$  varied from  $10^1$  to  $10^7 \Omega\text{-cm}^2$  for all PSC structures. All the PV parameters showed a similar pattern with increasing  $R_{Sh}$ , while the PV parameters increased rapidly from  $10^1$  to  $10^3 \Omega\text{-cm}^2$ . Especially, according to Figure 10a,  $\text{TiO}_2$  and ZnO as an ETL-associated structures showed a higher  $V_{OC}$  of 0.9 V but the other four ETL-associated structures showed an almost increasing pattern until 0.8 V. From Figure 10b, we observe that  $WS_2$  and  $C_{60}$  as ETL structures exhibit low  $J_{SC}$  among the other four structures, which were almost <12  $\text{mA}/\text{cm}^2$ . However, PCBM,  $\text{TiO}_2$ , and ZnO as ETL-based structures showed >12  $\text{mA}/\text{cm}^2$ , while the variation of  $R_{Sh}$  for  $\text{TiO}_2$ , ZnO, and IGZO as ETL-associated structures showed >16  $\text{mA}/\text{cm}^2$ . All the PSC structures showed increasing  $J_{SC}$  for  $R_{Sh}$  and became constant after  $\leq 10^3 \Omega\text{-cm}^2$ . In the case of FF, according to Figure 10c, all six PSC structures showed an increasing pattern, but  $\text{TiO}_2$  and ZnO as ETL-associated PSC structures showed almost 80% FF after diminishing  $R_{Sh}$  variation. All other four ETLs-associated PSC structures

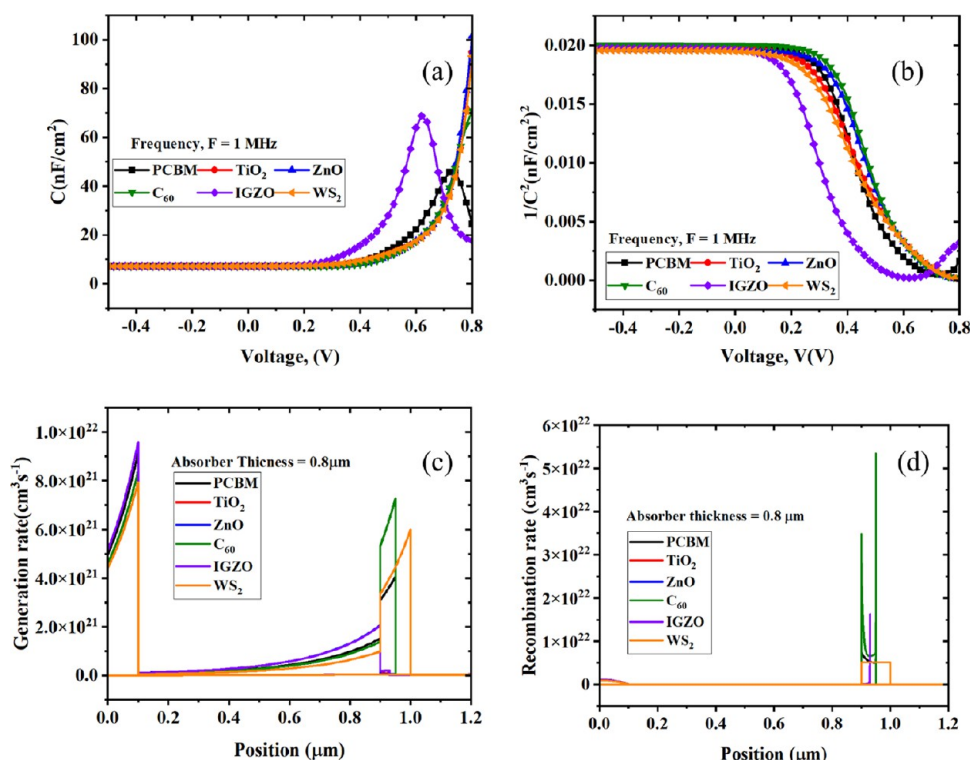


**Figure 12.** (a) Capacitance, (b) Mott–Schottky plot, (c) generation rate, and (d) recombination rate for the  $\text{CsPbBr}_3$  perovskite solar cell.

showed <80% of FF. The almost same pattern was observed in the case of PCE according to Figure 10d, in the case of  $\text{ZnO}$ , and  $\text{TiO}_2$  as the ETL-associated structure shows a higher PCE of almost >12%, and the other four PCE structures showed <12% of PCE.

**3.2.6. Effect of Temperature.** The temperature-induced performance losses caused by the incoming solar radiation, which also have an impact on the system's overall performance, have an impact on charge extraction. The mismatch between the thermal expansion coefficients and the low fracture energy of the layers has been proven to have an effect on the mechanical integrity of perovskite solar cells in earlier studies.<sup>69</sup> Solar concentration accelerates the rise in temperature inside the PSC while increasing the number of photons hitting the solar cell.<sup>70</sup> In concentrator photovoltaic devices, the increased light amplifies the photogenerated current, which converts the incoming radiation into electrical power. The dark current, which is a function of the operating temperature of the solar cell, lowers the  $V_{\text{OC}}$  and subsequently lowers the power production from the system. Since it makes up 80–90% of the temperature coefficient of efficiency, the open-circuit voltage's temperature sensitivity is crucial.<sup>71</sup> Figure 11 shows the effect of temperature from 275 to 475 K on the performance parameters of  $\text{CsPbBr}_3$ -based solar cells. According to Figure 11a,  $V_{\text{OC}}$  showed a decreasing pattern for both solar cell structures, with HTL in all six cases concerning increasing temperature; this is due to the increased saturation current. A slightly increasing  $J_{\text{SC}}$  pattern was observed from Figure 11b for  $\text{TiO}_2$ ,  $\text{ZnO}$ , and IGZO as ETL-associated PSC mode showed almost >16  $\text{mA}/\text{cm}^2 J_{\text{SC}}$  at the beginning of temperature variation, which is owing to the thermal generation of carriers accompanied with a suitable band gap, but the other three showed almost <16  $\text{mA}/\text{cm}^2 J_{\text{SC}}$ , which was lower than the first three structures  $\text{TiO}_2$ , IGZO, and  $\text{ZnO}$  ETL.

Furthermore, by observing Figure 11c with increasing temperature, FF showed a decreasing pattern in the cases of  $\text{ITO}/\text{TiO}_2/\text{CsPbBr}_3/\text{CFTS}/\text{Au}$ ,  $\text{ITO}/\text{C}_{60}/\text{CsPbBr}_3/\text{CFTS}/\text{Au}$ ,  $\text{ITO}/\text{IGZO}/\text{CsPbBr}_3/\text{CFTS}/\text{Au}$ , and  $\text{ITO}/\text{WS}_2/\text{CsPbBr}_3/\text{CFTS}/\text{Au}$ , but PCBM and  $\text{ZnO}$  as ETL-associated PSC structures showed an initially slightly increasing pattern; this is due to the impact of temperature on a material's effective band gap as well as carrier density and mobility in the device. Initially, according to Figure 11c,  $\text{TiO}_2$  as an ETL-associated solar cell showed a higher FF of about 90%, while the other five structures showed an FF of less than 90%, and the FF decreased throughout the temperature. Additionally, the PCE pattern shows a decreasing nature with respect to temperature in the case of six solar cell structures. According to Figure 11d, it is seen that initially,  $\text{TiO}_2$  and  $\text{ZnO}$  as ETL-associated mode showed almost 15% PCE while the other four ETL showed about <15% PCE, which almost reduced efficiency.

In Figure 11, with the temperature change, the changing trend of the parameters of solar cells with different transport layers is different. Some rise with the increase in temperature, some decline, and some remain unchanged. The PV parameters that rise with the increasing temperature is likely due to an increase in the carrier concentration and mobility within the solar cell. As the temperature increases, the number of carriers in the solar cell increases, leading to a higher carrier concentration. Additionally, the mobility of the carriers typically increases with temperature, resulting in more efficient charge transport and higher performance. The PV parameters decline with increasing temperature; this may be due to an increase in recombination processes, which reduces the efficiency of the solar cell. With higher temperatures, there is typically an increase in the rate of carrier recombination, leading to a decrease in the efficiency of the solar cell. Finally,

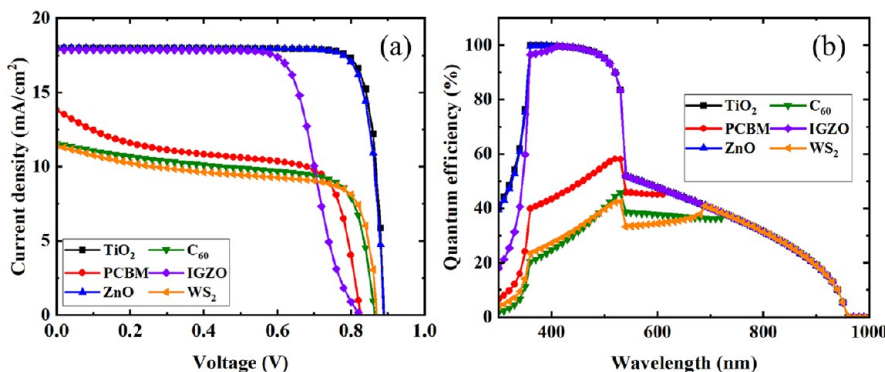


**Figure 13.** (a)  $J$ – $V$  characteristics and (b) quantum efficiency (QE) curve of  $\text{CsPbBr}_3$  PSCs.

for the parameters that remain unchanged with temperature, this may be due to a balance between the competing effects of increased carrier generation and increased recombination. In these cases, any increase in carrier generation due to higher temperatures is balanced by a corresponding increase in recombination, resulting in no net change in the solar cell parameters.

**3.2.7. Effect of Capacitance and Mott–Schottky.** Figure 12a,b depicts the differences in capacitance and Mott–Schottky (MS) values for the six PSCs when the voltage was increased from  $-0.5$  to  $0.8$  V and the frequency was constant at 1 MHz. In Figure 12a, IGZO, WS<sub>2</sub>, and ZnO as ETL-associated PSC structures showed exponentially increasing capacitance after  $0.4$  V except for the other three structures. The MS analysis (Figure 12b) focusing on capacitance–voltage metrics is a well-established experimental technique for analyzing space charge distributions in semiconductors, such as those caused by junction capacitance. Like capacitance, MS values of PCBM-based ETLs were declining after a certain voltage, while another device tends to decline after  $0.3$  V as a PCBM-based structure. The C–V behavior can be understood by integrating the Poisson equation (eq 8) and viewing the device as a plate capacitor.

$$C_D = \left[ \frac{-2\epsilon_s(v - v_{bi})}{qN_D} \right]^{1/2} \quad (8)$$

According to eq 8, it is feasible to immediately estimate the minority doping concentration ( $N_D$ ) as well as variables like the built-in potential ( $V_{bi}$ ) from the MS analysis with the elementary charge  $q$ , the vacuum permittivity  $\epsilon_0$ , and the dielectric constant  $\epsilon_s = \epsilon_0\epsilon_r$ . The formation of a depletion layer in the bulk or at the interface, which satisfies the Mott–Schottky equation, is a precondition for clearly identifying the  $C^{-2}$  Mott–Schottky area.<sup>72</sup>

**3.2.8. Effect of Generation and Recombination Rates.** Figures 12c,d depicts the generation of carriers and the rate of recombination. When an electron is propelled from the valence band to the conduction band during the carrier production process, as shown in Figure 12c, a hole is left in the valence band. As a result, electron–hole pairs are formed. Carrier production is caused by electron and hole emissions. At  $0.1$  and  $0.9$   $\mu\text{m}$ , the devices showed generation peaks, while at  $0.1$   $\mu\text{m}$ , they showed a higher generation rate than  $0.9$   $\mu\text{m}$ . SCAPS-1D calculates the formation of electron–hole pair generation based on the incoming photon flux  $N_{\text{phot}}(x)$ .  $G(x)$  can be calculated from this photon flow using eq 9.<sup>54</sup>

$$G(\lambda, x) = \alpha(\lambda, x) \times N_{\text{phot}}(\lambda, x) \quad (9)$$

Recombination is the opposite of generation in that it includes the joining and splitting of the electrons and holes in the conduction band. The lifetime and density of the charge carrier have an impact on the rate of recombination in a solar cell. Electron–hole recombination has decreased as a result of the defect states that are present in the absorber layer. The profile of electron–hole recombination inside the solar cell is affected by the creation of energy states. Because of flaws and grain boundaries, the recombination rate distribution is not uniform.<sup>54</sup>

**3.2.9.  $J$ – $V$  and QE Characteristics.** Figure 13a describes the  $J$ – $V$  characteristic curve of ITO/PCBM/CsPbBr<sub>3</sub>/CFTS/Au, ITO/TiO<sub>2</sub>/CsPbBr<sub>3</sub>/CFTS/Au, ITO/ZnO/CsPbBr<sub>3</sub>/CFTS/Au, ITO/C<sub>60</sub>/CsPbBr<sub>3</sub>/CFTS/Au, ITO/IGZO/CsPbBr<sub>3</sub>/CFTS/Au, and ITO/WS<sub>2</sub>/CsPbBr<sub>3</sub>/CFTS/Au solar cell structures. According to Figure 13a, it was observed that TiO<sub>2</sub> and ZnO as ETL-associated PSC structures showed a  $J_{\text{SC}}$  of almost  $17$  mA/cm<sup>2</sup> when the  $V_{\text{OC}}$  was about  $<0.9$  V, while the IGZO ETL-associated structure showed a  $J_{\text{SC}}$  of  $17$  mA/cm<sup>2</sup> when the voltage is near  $0.8$  V. Also, the PCBM ETL-associated structure showed a current density of  $<15$  mA/cm<sup>2</sup> when  $V_{\text{OC}}$  was about  $0$  to  $0.84$  V. When  $V_{\text{OC}}$  was  $>0.7$  V, WS<sub>2</sub> and C<sub>60</sub> as the ETL-associated structure showed reducing  $J_{\text{SC}}$ . When perovskite films have defect states, all photovoltaic parameters are significantly decreased. This is in line with the finding that substantial crystallinity in perovskite lowers charge recombination and improves performance.<sup>73</sup>

The QE curve for a variable wavelength is shown in Figure 13b. When the wavelength was near  $>300$  nm, the TiO<sub>2</sub>, ZnO, and IGZO as ETL with PSC had the best QE of  $100\%$  and PCBM as the ETL-associated structure showed  $60\%$  QE, while C<sub>60</sub> and WS<sub>2</sub> as the ETL-associated structure showed  $40\%$  QE when the wavelength was about  $500$  nm. When charge carriers are unable to enter an external circuit, recombination reduces the QE for the majority of solar cells. The QE is influenced by the same variables that influence collection probability. For example, changing the front surface could have an influence on carriers made near the surface. Free carrier absorption from highly doped front surface layers can reduce QE at longer wavelengths.<sup>74</sup>

CsPbBr<sub>3</sub> has a Shockley–Queisser (SQ) limit for a  $J_{\text{SC}}$  of  $8.96$  mA cm<sup>-2</sup>, as reported in the literature.<sup>75,76</sup> However, in our solar cell configuration, we used CFTS as the hole transport layer (HTL), which has a band gap of  $1.3$  eV, as shown in Table 2. This band gap value falls within the appropriate range for an absorber layer in a solar cell.<sup>76</sup> It is

**Table 5.** PV Parameters Comparison of CsPbI<sub>3</sub>-Based Solar Cells<sup>a</sup>

type	device structure	Voc (V)	Jsc (mA/cm <sup>2</sup> )	FF (%)	PCE (%)	year	ref
1	m-TiO <sub>2</sub> /CQD/CsPbBr <sub>3</sub> IO/spiro/Ag	1.06	11.34	69	8.29	2017	92
1	FTO/a-Nb <sub>2</sub> O <sub>5</sub> /CsPbBr <sub>3</sub> /CuPc/carbon	1.45	5.64	70	5.74	2019	18
1	FTO/TiO <sub>2</sub> /CsPbBr <sub>3</sub> /Spiro-OMeTAD/Ag	1.12	7.04	68	5.36	2019	79
1	TiO <sub>2</sub> /CsPbBr <sub>3</sub> /CuPc/carbon	1.26	6.62	74	6.21	2018	80
1	m-TiO <sub>2</sub> /GQDs/CsPbBr <sub>3</sub> /carbon	1.46	8.12	82	9.72	2018	93
1	FTO/TiO <sub>2</sub> /I-CsPbBr <sub>3</sub> /carbon	1.29	7.07	59	5.38	2019	82
1	FTO/mp-TiO <sub>2</sub> /CsPbBr <sub>3</sub>	1.27	6.13	57	4.43	2020	83
1	FTO/GQDs/CsPbBr <sub>3</sub> /PQDs/carbon	1.21	5.08	67	4.10	2018	84
1	FTO/c-TiO <sub>2</sub> /m-TiO <sub>2</sub> /CsPbBr <sub>3</sub> /NiO <sub>x</sub> /carbon	1.40	6.84	76	7.29	2018	85
1	m-TiO <sub>2</sub> /GQDs/CsPbBr <sub>3</sub> /CISZ-QDs/ carbon	1.52	7.35	84	9.43	2018	86
1	m-TiO <sub>2</sub> /CsPbBr <sub>3</sub> /carbon	1.24	7.4	73	6.70	2016	78
1	FTO/c-TiO <sub>2</sub> /Sn doped CsPbBr <sub>3</sub> /carbon	1.36	9.27	71	8.95	2021	87
1	m-TiO <sub>2</sub> /CsPbBr <sub>3</sub> /PTAA/Au	1.28	6.24	74	5.95	2020	77
1	FTO/TiO <sub>2</sub> /CsPbBr <sub>3</sub> /MoS <sub>2</sub> QDs	1.31	6.55	79	6.80	2018	88
1	FTO/TiO <sub>2</sub> /CsPbBr <sub>3</sub> + 3% L-Lysine/carbon	1.57	7.64	81	9.68	2020	89
2	ITO/GO/CsPbBr <sub>3</sub> /PEDOT:PSS/Au	1.57	8.50	77	10.34	2021	94
2	FTO/TiO <sub>2</sub> /CsPbBr <sub>3</sub> /Spiro-OMeTAD	1.68	8.17	84	11.58	2020	95
2	FTO/TiO <sub>2</sub> /CsPbBr <sub>3</sub> /NiO/Au	1.11	8.65	42	4.04	2019	96
2	ITO/PCBM/CsPbBr <sub>3</sub> /CFTS/Au	0.83	13.80	60.13	6.86	*	
2	ITO/ZnO/CsPbBr <sub>3</sub> /CFTS/Au	0.90	17.98	86	13.72	*	
2	ITO/C <sub>60</sub> /CsPbBr <sub>3</sub> /CFTS/Au	0.86	11.55	68	6.80	*	
2	ITO/IGZO/CsPbBr <sub>3</sub> /CFTS/Au	0.82	17.87	71.44	10.53	*	
2	ITO/WS <sub>2</sub> /CsPbBr <sub>3</sub> /CFTS/Au	0.87	11.43	67	6.66	*	
2	ITO/TiO <sub>2</sub> /CsPbBr <sub>3</sub> /CFTS/Au	0.89	17.98	87	13.86	*	

<sup>a</sup>1, Experimental; 2, theoretical, \*, this work.

important to note that CsPbBr<sub>3</sub> has a cut-off wavelength of  $\lambda_{\text{CsPbBr}_3} = 1.24/E_g$  (539 nm), while CFTS has a cut-off wavelength of  $\lambda_{\text{CFTS}} = 1.24/E_g$  (954 nm) for photon absorption. Therefore, photons with a wavelength shorter than 539 nm are absorbed in the perovskite layer, while photons with a longer wavelength are transmitted by the perovskite and are utilized by the CFTS. As a result, electron-hole pairs are generated in both the perovskite and CFTS layers due to photon absorption. These generated e-h pairs contribute to the overall  $J_{\text{SC}}$ , which is simulated to exceed 17 mA cm<sup>-2</sup>. The EQE response reported in Figure 13b confirms this behavior, showing a dip in EQE near 539 nm (due to the cut-off in perovskite absorption) and an extended response up to 954 nm (due to absorption in CFTS). This suggests that the enhanced  $J_{\text{SC}}$  is a result of the contribution of photon absorption by both perovskite and CFTS layers. It is also worth noting that CFTS with a band gap of 1.3 eV has an SQ limit of  $J_{\text{SC}}$  of 35.82 mA cm<sup>-2</sup>.<sup>76</sup>

**3.3. Comparison of SCAPS-1D Results with Previous Works.** Table 5 compares the performance characteristics of the presented CsPbBr<sub>3</sub>-based solar cell device designs to those of optimum configurations previously published. Table 5 demonstrates that the optimal CsPbBr<sub>3</sub> PSC cell offered a higher PCE value than the CsPbBr<sub>3</sub> device structure previously disclosed. PCE for desired CsPbBr<sub>3</sub>-based devices is 13.86%, compared to 5.95% for previously described device architectures like m-TiO<sub>2</sub>/CsPbBr<sub>3</sub>/PTAA/Au<sup>77</sup> and m-TiO<sub>2</sub>/CsPbBr<sub>3</sub>/carbon structure showing around 6.7% PCE.<sup>78</sup> The  $V_{\text{OC}}$  values of the solar structures are shown in line with the published device configurations. As opposed to the previously reported CsPbBr<sub>3</sub>-based device structure, the given solar structure has higher  $J_{\text{SC}}$  and FF values. It is seen that there are some differences between the calculated  $J_{\text{sc}}$  and  $V_{\text{oc}}$  values in the reported experimental results in the litera-

ture.<sup>77,78,87–89,79–86</sup> The possible reason might be that our studied ETLs and HTLs are not matched with previously studied experimental ones<sup>77,78,87–89,79–86</sup> as per their properties as well. Furthermore, optical properties also vary from absorber to absorber, which leads to solar energy absorption. In our study, ETL exhibits better performance according to their JV and QE characteristics because this ETL incorporates better band alignment in comparison to other respective ETLs, though some pieces of literature show that there is a large energy barrier between the conduction bands of TiO<sub>2</sub> and CsPbBr<sub>3</sub>.<sup>90,91</sup> The possible reason might be for another two important factors: the carrier mobility and transparency of the ETL, which can affect the device performance. The mobility of the charge carriers in the ETL can impact the efficiency of charge extraction and transport, and therefore the overall device performance. In general, ETLs with higher mobility can lead to better device performance. TiO<sub>2</sub> is a commonly used ETL material due to its high mobility, which allows for efficient charge extraction and transport. In addition, the transparency of the ETL can also affect the device's performance. A transparent ETL can allow more light to reach the perovskite absorber, leading to higher photon absorption and higher current output. TiO<sub>2</sub> has high transparency in the visible region, which is important for maximizing the light absorption in the perovskite absorber.

#### 4. SUMMARY

In this study, the structural, optical, and electronic aspects of the CsPbBr<sub>3</sub> absorber have been investigated using DFT simulations to support the photovoltaic applications of the titled compound. The calculated band gap (1.793 eV) of the CsPbBr<sub>3</sub> absorber using GGA-PBE approximation excellently matched with previous DFT calculated results. Additionally, it was shown by the charge density map and DOS that the Pb

6s/p orbital is the main contributor to the Pb atom's contribution. The  $\text{CsPbBr}_3$  perovskite is multiband in nature, as evidenced by the detection of a surface that mimics a Fermi surface for holes and electrons. Furthermore, a theoretical study of  $\text{CsPbBr}_3$ -based PSC is conducted in this research utilizing SCAPS-1D, where  $\text{CsPbBr}_3$  works as a light-harvesting layer while most studied HTLs and ETLs used to determine the most effective solar cell structures. Among the 54 combinations of the solar cell, structures were examined where the six best solar cell structures were triggered, namely, ITO/PCBM/ $\text{CsPbBr}_3$ /CFTS/Au, ITO/TiO<sub>2</sub>/ $\text{CsPbBr}_3$ /CFTS/Au, ITO/ZnO/ $\text{CsPbBr}_3$ /CFTS/Au, ITO/C<sub>60</sub>/ $\text{CsPbBr}_3$ /CFTS/Au, ITO/IGZO/ $\text{CsPbBr}_3$ /CFTS/Au, and ITO/WS<sub>2</sub>/ $\text{CsPbBr}_3$ /CFTS/Au. The following conclusion could be drawn by comparison of these six best structures:

- (i) Among the best structures, the ITO/TiO<sub>2</sub>/ $\text{CsPbBr}_3$ /CFTS/Au structure showed the highest PCE of 13.86%, and the ITO/WS<sub>2</sub>/ $\text{CsPbBr}_3$ /CFTS/Au structure showed the lowest PCE of 6.66%.
- (ii) In the case of the absorber and ETL thickness impact on respective structures, ITO/TiO<sub>2</sub>/ $\text{CsPbBr}_3$ /CFTS/Au showed parallel performance of 14% in between absorber and ETL thicknesses of 1–1.3 and 0.1–0.15  $\mu\text{m}$ , respectively.
- (iii) Considering the effect of series resistance, shunt resistance, and operating temperature, the ITO/TiO<sub>2</sub>/ $\text{CsPbBr}_3$ /CFTS/Au structure outperformed other studied devices.  $V_{\text{oc}}$  and  $J_{\text{sc}}$  show an almost independent nature concerning series resistance, whereas shunt resistance shows an almost proportional relation with the performance parameters.
- (iv) The PCBM ETL-associated structure showed an increasing capacitance of 50 C at 0.7 V; on the other hand, ZnO ETL showed a maximum of 100 C with the built-in voltage increases. However, the PCBM ETL structure MS value also declined while other ETLs tend to decline after 0.4 V except for the IGZO ETL-associated structure.
- (v) The IGZO ETL-associated structure incorporates the highest generation rate at the position of 0.1  $\mu\text{m}$ , whereas the C<sub>60</sub> ETL-associated structure produced the highest recombination rate in between the position 0.9 to 1  $\mu\text{m}$ .
- (vi) TiO<sub>2</sub> ETL exhibits better performance according to their JV and QE characteristics, which might be due to the better transparency and charge carriers mobility of TiO<sub>2</sub> in comparison to other respective ETLs.

Therefore, this numerical investigation also helped identify the ideal ITO/ETL/ $\text{CsPbBr}_3$ /HTL/Au combination as a template for experimentally redesigning a low-cost, dependable, and highly functional  $\text{CsPbBr}_3$ -based PSC since it is difficult to evaluate all potential combinations. To develop a better combination for  $\text{CsPbBr}_3$ -based PSC in the future, it can be suggested to use machine learning in this effort.

## ASSOCIATED CONTENT

### Data Availability Statement

The raw/processed data required to reproduce these findings cannot be shared at this time as the data also forms part of an ongoing study.

## AUTHOR INFORMATION

### Corresponding Authors

**M. Khalid Hossain** — Institute of Electronics, Atomic Energy Research Establishment, Bangladesh Atomic Energy Commission, Dhaka 1349, Bangladesh; Department of Advanced Energy Engineering Science, Interdisciplinary Graduate School of Engineering Sciences, Kyushu University, Fukuoka 816-8580, Japan;  [orcid.org/0000-0003-4595-6367](https://orcid.org/0000-0003-4595-6367); Email: [khalid.baec@gmail.com](mailto:khalid.baec@gmail.com), [khalid@kyudai.jp](mailto:khalid@kyudai.jp)

**Mustafa K. A. Mohammed** — University of Warith Al-Anbiyaa, 56001 Karbala, Iraq; Email: [mustafa\\_kareem97@yahoo.com](mailto:mustafa_kareem97@yahoo.com)

### Authors

**Rahul Pandey** — VLSI Centre of Excellence, Chitkara University Institute of Engineering and Technology, Chitkara University, Punjab 140401, India;  [orcid.org/0000-0001-7766-3572](https://orcid.org/0000-0001-7766-3572)

**A. A. Arnab** — Department of Electrical & Electronic Engineering, Ahsanullah University of Science and Technology, Dhaka 1208, Bangladesh

**M. H. K. Rubel** — Department of Materials Science and Engineering, University of Rajshahi, Rajshahi 6205, Bangladesh;  [orcid.org/0000-0001-9420-4335](https://orcid.org/0000-0001-9420-4335)

**K. M. Hossain** — Department of Materials Science and Engineering, University of Rajshahi, Rajshahi 6205, Bangladesh

**Md Hasan Ali** — Department of Electrical and Electronic Engineering, Begum Rokeya University, Rangpur 5400, Bangladesh

**Md. Ferdous Rahman** — Department of Electrical and Electronic Engineering, Begum Rokeya University, Rangpur 5400, Bangladesh

**H. Bencherif** — LEREESI, Higher National School of Renewable Energies, Environment and Sustainable Development, Batna 05078, Algeria

**Jaya Madan** — VLSI Centre of Excellence, Chitkara University Institute of Engineering and Technology, Chitkara University, Punjab 140401, India

**Md. Rasidul Islam** — Department of Electrical and Electronic Engineering, Bangamata Sheikh Fojilatunnesa Mujib Science & Technology University, Jamalpur 2012, Bangladesh

**D. P. Samajdar** — Dept. of ECE, Indian Institute of Information Technology, Design & Manufacturing, Madhya Pradesh 482005, India;  [orcid.org/0000-0001-9518-2692](https://orcid.org/0000-0001-9518-2692)

**Sagar Bhattacharai** — Department of Physics, Arunachal University of Studies, Namsai 792103 Arunachal Pradesh, India

Complete contact information is available at:  
<https://pubs.acs.org/10.1021/acs.energyfuels.3c00035>

### Notes

The authors declare no competing financial interest.

## ACKNOWLEDGMENTS

The SCAPS-1D program was kindly provided by Dr. M. Burgelman of the University of Gent in Belgium. The authors would like to express their gratitude to him.

## REFERENCES

- (1) Green, M. A.; Ho-Baillie, A.; Snaith, H. J. The Emergence of Perovskite Solar Cells. *Nat. Photonics* **2014**, *8*, 506–514.

- (2) Shrivastav, N.; Kashyap, S.; Madan, J.; Al-Mousoi, A. K.; Mohammed, M. K. A.; Hossain, M. K.; Pandey, R.; Ramanujam, J. Perovskite-CIGS Monolithic Tandem Solar Cells with 29.7% Efficiency: A Numerical Study. *Energy Fuels* **2023**, *37*, 3083–3090.
- (3) Kashyap, S.; Madan, J.; Mohammed, M. K. A.; Hossain, M. K.; Ponnusamy, S.; Pandey, R. Unlocking the Potential of MgF<sub>2</sub> Textured Surface in Enhancing the Efficiency of Perovskite Solar Cells. *Mater. Lett.* **2023**, *339*, No. 134096.
- (4) Dureja, T.; Garg, A.; Bhalla, S.; Bhutani, D.; Khanna, A. Double Lead-Free Perovskite Solar Cell for 19.9% Conversion Efficiency: A SCAPS-1D Based Simulation Study. *Mater. Today: Proc.* **2022**, *71*, 239–242.
- (5) Xing, G.; Mathews, N.; Sun, S.; Lim, S. S.; Lam, Y. M.; Grätzel, M.; Mhaisalkar, S.; Sum, T. C. Long-Range Balanced Electron-and Hole-Transport Lengths in Organic-Inorganic CH<sub>3</sub>NH<sub>3</sub>PbI<sub>3</sub>. *Science* **2013**, *342*, 344–347.
- (6) National Renewable Energy Laboratory. *Best Research-Cell Efficiency Chart*; U.S. Department of Energy. <https://www.nrel.gov/pv/cell-efficiency.html> (accessed 2022-12-04).
- (7) Conings, B.; Drijkoningen, J.; Gauquelin, N.; Babayigit, A.; D'Haen, J.; D'Olieslaeger, L.; Ethirajan, A.; Verbeeck, J.; Manca, J.; Mosconi, E.; Angelis, F. D.; Boyen, H.-G. Intrinsic Thermal Instability of Methylammonium Lead Trihalide Perovskite. *Adv. Energy Mater.* **2015**, *5*, 1500477.
- (8) Thakur, A.; Singh, D.; Gill, S. K. Numerical Simulations of 26.11% Efficient Planar CH<sub>3</sub>NH<sub>3</sub>PbI<sub>3</sub> Perovskite n-i-p Solar Cell. *Mater. Today: Proc.* **2022**, *71*, 195–201.
- (9) Ava, T. T.; Al Mamun, A.; Marsillac, S.; Namkoong, G. A Review: Thermal Stability of Methylammonium Lead Halide Based Perovskite Solar Cells. *Appl. Sci.* **2019**, *9*, 188.
- (10) Dong, C.; Han, X.; Li, W.; Qiu, Q.; Wang, J. Anti-Solvent Assisted Multi-Step Deposition for Efficient and Stable Carbon-Based CsPbI<sub>3</sub>Br All-Inorganic Perovskite Solar Cell. *Nano Energy* **2019**, *59*, 553–559.
- (11) Wang, Y.; Liu, X.; Zhou, Z.; Ru, P.; Chen, H.; Yang, X.; Han, L. Reliable Measurement of Perovskite Solar Cells. *Adv. Mater.* **2019**, *31*, 1803231.
- (12) Pandey, R.; Bhattacharai, S.; Sharma, K.; Madan, J.; Al-Mousoi, A. K.; Mohammed, M. K. A.; Hossain, M. K. Halide Composition Engineered a Non-Toxic Perovskite–Silicon Tandem Solar Cell with 30.7% Conversion Efficiency. *ACS Appl. Electron. Mater.* **2023**, DOI: [10.1021/acsaem.2c01574](https://doi.org/10.1021/acsaem.2c01574).
- (13) Dastidar, S.; Egger, D. A.; Tan, L. Z.; Cromer, S. B.; Dillon, A. D.; Liu, S.; Kronik, L.; Rappe, A. M.; Fafarman, A. T. High Chloride Doping Levels Stabilize the Perovskite Phase of Cesium Lead Iodide. *Nano Lett.* **2016**, *16*, 3563–3570.
- (14) Tong, G.; Ono, L. K.; Qi, Y. Recent Progress of All-Bromide Inorganic Perovskite Solar Cells. *Energy Technol.* **2020**, *8*, 1900961.
- (15) Ghaithan, H. M.; Alahmed, Z. A.; Qaid, S. M. H.; Hezam, M.; Aldwayyan, A. S. Density Functional Study of Cubic, Tetragonal, and Orthorhombic CsPbBr<sub>3</sub> Perovskite. *ACS Omega* **2020**, *5*, 7468–7480.
- (16) Tidrow, S. C. Mapping Comparison of Goldschmidt's Tolerance Factor with Perovskite Structural Conditions. *Ferroelectrics* **2014**, *470*, 13–27.
- (17) Stranks, S. D.; Eperon, G. E.; Grancini, G.; Menelaou, C.; Alcocer, M. J. P.; Leijtens, T.; Herz, L. M.; Petrozza, A.; Snaith, H. J. Electron-Hole Diffusion Lengths Exceeding 1 Micrometer in an Organometal Trihalide Perovskite Absorber. *Science* **2013**, *342*, 341–344.
- (18) Zhao, F.; Guo, Y.; Wang, X.; Tao, J.; Jiang, J.; Hu, Z.; Chu, J. Enhanced Performance of Carbon-Based Planar CsPbBr<sub>3</sub> Perovskite Solar Cells with Room-Temperature Sputtered Nb<sub>2</sub>O<sub>5</sub> Electron Transport Layer. *Sol. Energy* **2019**, *191*, 263–271.
- (19) Hossain, M. K.; Toki, G. F. I.; Kuddus, A.; Rubel, M. H. K.; Hossain, M. M.; Bencherif, H.; Rahman, M. F.; Islam, M. R.; Mushtaq, M. An Extensive Study on Multiple ETL and HTL Layers to Design and Simulation of High-Performance Lead-Free CsSnCl<sub>3</sub>-Based Perovskite Solar Cells. *Sci. Rep.* **2023**, *13*, 2521.
- (20) Hossain, M. K.; Samajdar, D. P.; Das, R. C.; Arnab, A. A.; Rahman, M. F.; Rubel, M. H. K.; Islam, M. R.; Bencherif, H.; Pandey, R.; Madan, J.; Mohammed, M. K. A. Design and Simulation of Cs<sub>2</sub>BiAgI<sub>6</sub> Double Perovskite Solar Cells with Different Electron Transport Layers for Efficiency Enhancement. *Energy Fuels* **2023**, *37*, 3957–3979.
- (21) Basher, M. K.; Shah Riyadh, S. M.; Hossain, M. K.; Hassan, M.; Akand, M. A. R.; Amir-Al Zumahi, S. M.; Matin, M. A.; Das, N.; Nur-E-Alam, M. Development of Zinc-Oxide Nanorods on Chemically Etched Zinc Plates Suitable for High-Efficiency Photovoltaics Solar Cells. *Opt. Quantum Electron.* **2023**, *55*, 322.
- (22) Chen, J.; Park, N.-G. Inorganic Hole Transporting Materials for Stable and High Efficiency Perovskite Solar Cells. *J. Phys. Chem. C* **2018**, *122*, 14039–14063.
- (23) Hossain, M. K.; Raihan, G. A.; Akbar, M. A.; Kabir Rubel, M. H.; Ahmed, M. H.; Khan, M. I.; Hossain, S.; Sen, S. K.; Jalal, M. I. E.; El-Denglawey, A. Current Applications and Future Potential of Rare Earth Oxides in Sustainable Nuclear, Radiation, and Energy Devices: A Review. *ACS Appl. Electron. Mater.* **2022**, *4*, 3327–3353.
- (24) Hossain, M. K.; Ahmed, M. H.; Khan, M. I.; Miah, M. S.; Hossain, S. Recent Progress of Rare Earth Oxides for Sensor, Detector, and Electronic Device Applications: A Review. *ACS Appl. Electron. Mater.* **2021**, *3*, 4255–4283.
- (25) Saurabh, S.; Hossain, M. K.; Singh, S.; Agnihotri, S. K.; Samajdar, D. P. Optical Performance Analysis of InP Nanostructures for Photovoltaic Applications. *RSC Adv.* **2023**, *13*, 9878–9891.
- (26) Khan, S.; Hossain, M. K. Classification and Properties of Nanoparticles. In *Nanoparticle-Based Polymer Composites*; Elsevier, 2022; pp. 15–54, DOI: [10.1016/B978-0-12-824272-8.00009-9](https://doi.org/10.1016/B978-0-12-824272-8.00009-9).
- (27) Hossain, M. K.; Hossain, S.; Ahmed, M. H.; Khan, M. I.; Haque, N.; Raihan, G. A. A Review on Optical Applications, Prospects, and Challenges of Rare-Earth Oxides. *ACS Appl. Electron. Mater.* **2021**, *3*, 3715–3746.
- (28) Hossain, M. K.; Rubel, M. H. K.; Akbar, M. A.; Ahmed, M. H.; Haque, N.; Rahman, M. F.; Hossain, J.; Hossain, K. M. A Review on Recent Applications and Future Prospects of Rare Earth Oxides in Corrosion and Thermal Barrier Coatings, Catalysts, Tribological, and Environmental Sectors. *Ceram. Int.* **2022**, *48*, 32588–32612.
- (29) Rubel, M. H. K.; Hossain, M. A.; Hossain, M. K.; Hossain, K. M.; Khatun, A. A.; Rahaman, M. M.; Ferdous Rahman, M.; Hossain, M. M.; Hossain, J. First-Principles Calculations to Investigate Structural, Elastic, Electronic, Thermodynamic, and Thermoelectric Properties of CaPd<sub>3</sub>B<sub>4</sub>O<sub>12</sub> (B = Ti, V) Perovskites. *Results Phys.* **2022**, *42*, No. 105977.
- (30) Islam, M. R.; Mazumder, A. A. M.; Mojumder, M. R. H.; Shifat, A. S. M. Z.; Hossain, M. K. Strain-Induced Tunable Optoelectronic Properties of Inorganic Halide Perovskites APbCl<sub>3</sub> (A = K, Rb, and Cs). *Jpn. J. Appl. Phys.* **2023**, *62*, No. 011002.
- (31) Hossain, M. K.; Arnab, A. A.; Das, R. C.; Hossain, K. M.; Rubel, M. H. K.; Rahman, M. F.; Bencherif, H.; Emetere, M. E.; Mohammed, M. K. A.; Pandey, R. Combined DFT, SCAPS-1D, and WxAMPS Frameworks for Design Optimization of Efficient Cs<sub>2</sub>BiAgI<sub>6</sub>-Based Perovskite Solar Cells with Different Charge Transport Layers. *RSC Adv.* **2022**, *12*, 34850–34873.
- (32) Mushtaq, M.; Algethami, N.; Khan, M. A. R.; Ayesh, A. I.; Mateen, M.; Laref, A.; Abdelmohsen, S. A. M.; Hossain, M. K. Adsorption of NO<sub>x</sub> (x=1, 2) Molecule on CoFeMnSi(001) Surface: First-Principles Insights. *ACS Omega* **2023**, DOI: [10.1021/acsomega.3c00569](https://doi.org/10.1021/acsomega.3c00569).
- (33) López, C. A.; Abia, C.; Alvarez-Galván, M. C.; Hong, B.-K.; Martínez-Huerta, M. V.; Serrano-Sánchez, F.; Carrascoso, F.; Castellanos-Gómez, A.; Fernández-Díaz, M. T.; Alonso, J. A. Crystal Structure Features of CsPbBr<sub>3</sub> Perovskite Prepared by Mechanochemical Synthesis. *ACS Omega* **2020**, *5*, 5931–5938.
- (34) Rajeswarapalanichamy, R.; Amudhavalli, A.; Padmavathy, R.; Iyakutti, K. Band Gap Engineering in Halide Cubic Perovskites CsPbBr<sub>3-y</sub>I<sub>y</sub> (y = 0, 1, 2, 3) – A DFT Study. *Mater. Sci. Eng., B* **2020**, *258*, No. 114560.

- (35) Najim, A.; Hartiti, B.; Absike, H.; Tchognia Nkuissi, H. J.; Labrim, H.; Fadili, S.; Thevenin, P.; Ertugrul, M. Theoretical Investigation of Structural, Electronic, and Optical Properties of Halide Cubic Perovskite  $\text{CsPbBr}_{3-x}\text{I}_x$ . *Mater. Sci. Semicond. Process.* **2022**, *141*, No. 106442.
- (36) Rubel, M. H. K.; Mitro, S. K.; Hossain, M. K.; Hossain, K. M.; Rahaman, M. M.; Hossain, J.; Mondal, B. K.; Akter, A.; Rahman, M. F.; Ahmed, I.; Islam, A. K. M. A. First-Principles Calculations to Investigate Physical Properties of Single-Cubic  $(\text{Ba}_{0.82}\text{K}_{0.18})_{(1-x)}(\text{Bi}_{0.53}\text{Pb}_{0.47})\text{O}_3$  Novel Perovskite Superconductor. *Mater. Today Commun.* **2022**, *33*, No. 104302.
- (37) Payne, M. C.; Teter, M. P.; Allan, D. C.; Arias, T. A.; Joannopoulos, J. D. Iterative Minimization Techniques for Ab Initio Total-Energy Calculations: Molecular Dynamics and Conjugate Gradients. *Rev. Mod. Phys.* **1992**, *64*, 1045–1097.
- (38) Segall, M. D.; Lindan, P. J. D.; Probert, M. J.; Pickard, C. J.; Hasnip, P. J.; Clark, S. J.; Payne, M. C. First-Principles Simulation: Ideas, Illustrations and the CASTEP Code. *J. Phys.: Condens. Matter* **2002**, *14*, 2717–2744.
- (39) Rohrer, G. S. *Structure and Bonding in Crystalline Materials*; Cambridge University Press, 2001.
- (40) Perdew, J. P.; Burke, K.; Ernzerhof, M. Generalized Gradient Approximation Made Simple. *Phys. Rev. Lett.* **1996**, *77*, 3865–3868.
- (41) Vanderbilt, D. Soft Self-Consistent Pseudopotentials in a Generalized Eigenvalue Formalism. *Phys. Rev. B* **1990**, *41*, 7892–7895.
- (42) Fischer, T. H.; Almlöf, J. General Methods for Geometry and Wave Function Optimization. *J. Phys. Chem.* **1992**, *96*, 9768–9774.
- (43) Monkhorst, H. J.; Pack, J. D. Special Points for Brillouin-Zone Integrations. *Phys. Rev. B* **1976**, *13*, 5188–5192.
- (44) Boekelheide, Z.; Saerbeck, T.; Stampfl, A. P. J.; Robinson, R. A.; Stewart, D. A.; Hellman, F. Antiferromagnetism in  $\text{Cr}_3\text{Al}$  and Relation to Semiconducting Behavior. *Phys. Rev. B* **2012**, *85*, No. 094413.
- (45) Collins, L. A.; Bickham, S. R.; Kress, J. D.; Mazeved, S.; Lenosky, T. J.; Troullier, N. J.; Windl, W. Dynamical and Optical Properties of Warm Dense Hydrogen. *Phys. Rev. B* **2001**, *63*, No. 184110.
- (46) Bencherif, H.; Hossain, M. K. Design and Numerical Investigation of Efficient  $(\text{FAPbI}_3)_{1-x}(\text{CsSnI}_3)_x$  Perovskite Solar Cell with Optimized Performances. *Sol. Energy* **2022**, *248*, 137–148.
- (47) Rahman, M. F.; Habib, M. J. A.; Ali, M. H.; Rubel, M. H. K. K.; Islam, M. R.; Md Ismail, A. B.; Hossain, M. K. Design and Numerical Investigation of Cadmium Telluride ( $\text{CdTe}$ ) and Iron Silicide ( $\text{FeSi}_2$ ) Based Double Absorber Solar Cells to Enhance Power Conversion Efficiency. *AIP Adv.* **2022**, *12*, 105317.
- (48) Bencherif, H.; Meddour, F.; Elshorbagy, M. H.; Hossain, M. K.; Cuadrado, A.; Abdi, M. A.; Bendib, T.; Kouda, S.; Alda, J. Performance Enhancement of  $(\text{FAPbI}_3)_{1-x}(\text{MAPbBr}_3)_x$  Perovskite Solar Cell with an Optimized Design. *Micro Nanostruct.* **2022**, *171*, No. 207403.
- (49) Rahman, M. F.; Moon, M. M. A.; Hossain, M. K.; Ali, M. H.; Haque, M. D.; Kuddus, A.; Hossain, J.; Ismail, M. A. B. Concurrent Investigation of Antimony Chalcogenide ( $\text{Sb}_2\text{Se}_3$  and  $\text{Sb}_2\text{S}_3$ )-Based Solar Cells with a Potential  $\text{WS}_2$  Electron Transport Layer. *Heliyon* **2022**, *8*, No. e12034.
- (50) Hossain, M. K.; Toki, G. F. I.; Alam, I.; Pandey, R.; Samajdar, D. P.; Rahman, M. F.; Islam, M. R.; Rubel, M. H. K.; Bencherif, H.; Madan, J.; Mohammed, M. K. A. Numerical Simulation and Optimization of a  $\text{CsPbI}_3$ -Based Perovskite Solar Cell to Enhance the Power Conversion Efficiency. *New J. Chem.* **2023**, *47*, 4801–4817.
- (51) Minbashi, M.; Ghobadi, A.; Ehsani, M. H.; Dizaji, H. R.; Memarian, N. Simulation of High Efficiency SnS-Based Solar Cells with SCAPS. *Sol. Energy* **2018**, *176*, 520–525.
- (52) Sze, S. M.; Ng, K. K. LEDs and Lasers. In *Physics of Semiconductor Devices*; John Wiley & Sons, Inc.: Hoboken, NJ, USA, 2006; pp. 599–662, DOI: [10.1002/9780470068328.ch12](https://doi.org/10.1002/9780470068328.ch12).
- (53) Zhang, M.; Zheng, Z.; Fu, Q.; Chen, Z.; He, J.; Zhang, S.; Chen, C.; Luo, W. Synthesis and Single Crystal Growth of Perovskite Semiconductor  $\text{CsPbBr}_3$ . *J. Cryst. Growth* **2018**, *484*, 37–42.
- (54) Hossain, M. K.; Rubel, M. H. K.; Toki, G. F. I.; Alam, I.; Rahman, M. F.; Bencherif, H. Effect of Various Electron and Hole Transport Layers on the Performance of  $\text{CsPbI}_3$ -Based Perovskite Solar Cells: A Numerical Investigation in DFT, SCAPS-1D, and WxAMPS Frameworks. *ACS Omega* **2022**, *7*, 43210–43230.
- (55) Sawicka-chudy, P.; Rybak-wilusz, E.; Cholewa, M. Review of the Development of Copper Oxides with Titanium Dioxide Thin-Film Solar Cells Review of the Development of Copper Oxides with Titanium Dioxide Thin-Film Solar Cells. *2020*, *10* January, 010701 DOI: [10.1063/1.5125433](https://doi.org/10.1063/1.5125433).
- (56) Roknuzzaman, M.; Ostrikov, K.; Wang, H.; Du, A.; Tesfamichael, T. Towards Lead-Free Perovskite Photovoltaics and Optoelectronics by Ab-Initio Simulations. *Sci. Rep.* **2017**, *7*, 14025.
- (57) Kholil, M. I.; Bhuiyan, M. T. H. Effects of Pressure on Narrowing the Band Gap, Visible Light Absorption, and Semi-Metallic Transition of Lead-Free Perovskite  $\text{CsSnBr}_3$  for Optoelectronic Applications. *J. Phys. Chem. Solids* **2021**, *154*, No. 110083.
- (58) Murtaza, G.; Ahmad, I. First Principle Study of the Structural and Optoelectronic Properties of Cubic Perovskites  $\text{CsPbM}_3$  ( $\text{M}=\text{Cl}, \text{Br}, \text{I}$ ). *Phys. B* **2011**, *406*, 3222–3229.
- (59) Afsari, M.; Boochani, A.; Hantezadeh, M.; Elahi, S. M. Topological Nature in Cubic Phase of Perovskite  $\text{CsPbI}_3$ : By DFT. *Solid State Commun.* **2017**, *259*, 10–15.
- (60) Khattak, Y. H.; Baig, F.; Toura, H.; Beg, S.; Soucase, B. M. CZTSe Kesterite as an Alternative Hole Transport Layer for  $\text{MASnI}_3$  Perovskite Solar Cells. *J. Electron. Mater.* **2019**, *48*, 5723–5733.
- (61) Ge, J.; Grice, C. R.; Yan, Y. Cu-Based Quaternary Chalcogenide  $\text{Cu}_2\text{BaSnS}_4$  Thin Films Acting as Hole Transport Layers in Inverted Perovskite  $\text{CH}_3\text{NH}_3\text{PbI}_3$  Solar Cells. *J. Mater. Chem. A* **2017**, *5*, 2920–2928.
- (62) Jung, E. H.; Jeon, N. J.; Park, E. Y.; Moon, C. S.; Shin, T. J.; Yang, T.-Y.; Noh, J. H.; Seo, J. Efficient, Stable and Scalable Perovskite Solar Cells Using Poly(3-Hexylthiophene). *Nature* **2019**, *567*, 511–515.
- (63) Bi, E.; Tang, W.; Chen, H.; Wang, Y.; Barbaud, J.; Wu, T.; Kong, W.; Tu, P.; Zhu, H.; Zeng, X.; He, J.; Kan, S.; Yang, X.; Grätzel, M.; Han, L. Efficient Perovskite Solar Cell Modules with High Stability Enabled by Iodide Diffusion Barriers. *Joule* **2019**, *3*, 2748–2760.
- (64) Bogachuk, D.; Tsuji, R.; Martineau, D.; Narbey, S.; Herterich, J. P.; Wagner, L.; Suginuma, K.; Ito, S.; Hinsch, A. Comparison of Highly Conductive Natural and Synthetic Graphites for Electrodes in Perovskite Solar Cells. *Carbon* **2021**, *178*, 10–18.
- (65) Rakocevic, L.; Mundt, L. E.; Gehlhaar, R.; Merckx, T.; Aernouts, T.; Schubert, M. C.; Glunz, S. W.; Poortmans, J. Loss Analysis in Perovskite Photovoltaic Modules. *Sol. RRL* **2019**, *3*, 1900338.
- (66) Galagan, Y.; Coenen, E. W. C.; Verhees, W. J. H.; Andriessen, R. Towards the Scaling up of Perovskite Solar Cells and Modules. *J. Mater. Chem. A* **2016**, *4*, 5700–5705.
- (67) Tvingstedt, K.; Gil-Escríg, L.; Momblona, C.; Rieder, P.; Kiermasch, D.; Sessolo, M.; Baumann, A.; Bolink, H. J.; Dyakonov, V. Removing Leakage and Surface Recombination in Planar Perovskite Solar Cells. *ACS Energy Lett.* **2017**, *2*, 424–430.
- (68) Li, Y.; Ding, B.; Chu, Q.-Q.; Yang, G.-J.; Wang, M.; Li, C.-X.; Li, C.-J. Ultra-High Open-Circuit Voltage of Perovskite Solar Cells Induced by Nucleation Thermodynamics on Rough Substrates. *Sci. Rep.* **2017**, *7*, 46141.
- (69) Baig, H.; Kanda, H.; Asiri, A. M.; Nazeeruddin, M. K.; Mallick, T. Increasing Efficiency of Perovskite Solar Cells Using Low Concentrating Photovoltaic Systems. *Sustainable Energy Fuels* **2020**, *4*, 528–537.
- (70) Checharoen, R.; Rolston, N.; Harwood, D.; Bush, K. A.; Dauskardt, R. H.; McGehee, M. D. Design and Understanding of Encapsulated Perovskite Solar Cells to Withstand Temperature Cycling. *Energy Environ. Sci.* **2018**, *11*, 144–150.
- (71) Green, M. A. General Temperature Dependence of Solar Cell Performance and Implications for Device Modelling. *Prog. Photovolt.: Res. Appl.* **2003**, *11*, 333–340.

- (72) Gelderman, K.; Lee, L.; Donne, S. W. Flat-Band Potential of a Semiconductor: Using the Mott–Schottky Equation. *J. Chem. Educ.* **2007**, *84*, 685.
- (73) Liu, M.; Johnston, M. B.; Snaith, H. J. Efficient Planar Heterojunction Perovskite Solar Cells by Vapour Deposition. *Nature* **2013**, *501*, 395–398.
- (74) Baker-Finch, S. C.; McIntosh, K. R.; Yan, D.; Fong, K. C.; Kho, T. C. Near-Infrared Free Carrier Absorption in Heavily Doped Silicon. *J. Appl. Phys.* **2014**, *116*, No. 063106.
- (75) Duan, J.; Xu, H.; Sha, W. E. I.; Zhao, Y.; Wang, Y.; Yang, X.; Tang, Q. Inorganic Perovskite Solar Cells: An Emerging Member of the Photovoltaic Community. *J. Mater. Chem. A* **2019**, *7*, 21036–21068.
- (76) Rühle, S. Tabulated Values of the Shockley–Queisser Limit for Single Junction Solar Cells. *Sol. Energy* **2016**, *130*, 139–147.
- (77) Kulbak, M.; Cahen, D.; Hodes, G. How Important Is the Organic Part of Lead Halide Perovskite Photovoltaic Cells? Efficient CsPbBr<sub>3</sub> Cells. *J. Phys. Chem. Lett.* **2015**, *6*, 2452–2456.
- (78) Liang, J.; Wang, C.; Wang, Y.; Xu, Z.; Lu, Z.; Ma, Y.; Zhu, H.; Hu, Y.; Xiao, C.; Yi, X.; Zhu, G.; Lv, H.; Ma, L.; Chen, T.; Tie, Z.; Jin, Z.; Liu, J. All-Inorganic Perovskite Solar Cells. *J. Am. Chem. Soc.* **2016**, *138*, 15829–15832.
- (79) Zhou, Z.-J.; Deng, Y.-Q.; Zhang, P.-P.; Kou, D.-X.; Zhou, W.-H.; Meng, Y.-N.; Yuan, S.-J.; Wu, S.-X. Cu<sub>2</sub>ZnSnS<sub>4</sub> Quantum Dots as Hole Transport Material for Enhanced Charge Extraction and Stability in All-Inorganic CsPbBr<sub>3</sub> Perovskite Solar Cells. *Sol. RRL* **2019**, *3*, 1800354.
- (80) Liu, Z.; Sun, B.; Liu, X.; Han, J.; Ye, H.; Shi, T.; Tang, Z.; Liao, G. Efficient Carbon-Based CsPbBr<sub>3</sub> Inorganic Perovskite Solar Cells by Using Cu-Phthalocyanine as Hole Transport Material. *Nano-Micro Lett.* **2018**, *10*, 34.
- (81) Zhou, S.; Shen, S.; Fang, X.; Hou, Q.; Zhao, D. An Accurate and Rapid Method to Compare Thermal Insulation Capacity of Nine Gd-Yb-YSZ Coatings. *Ceram. Int.* **2019**, *45*, 19910–19917.
- (82) Liu, J.; Zhu, L.; Xiang, S.; Wei, Y.; Xie, M.; Liu, H.; Li, W.; Chen, H. Growing High-Quality CsPbBr<sub>3</sub> by Using Porous CsPb<sub>2</sub>Br<sub>5</sub> as an Intermediate: A Promising Light Absorber in Carbon-Based Perovskite Solar Cells. *Sustainable Energy Fuels* **2019**, *3*, 184–194.
- (83) Lee, E. J.; Kim, D.-H.; Chang, R. P. H.; Hwang, D.-K. Induced Growth of CsPbBr<sub>3</sub> Perovskite Films by Incorporating Metal Chalcogenide Quantum Dots in PbBr<sub>2</sub> Films for Performance Enhancement of Inorganic Perovskite Solar Cells. *ACS Appl. Energy Mater.* **2020**, *3*, 10376–10383.
- (84) Duan, J.; Zhao, Y.; He, B.; Tang, Q. Simplified Perovskite Solar Cell with 4.1% Efficiency Employing Inorganic CsPbBr<sub>3</sub> as Light Absorber. *Small* **2018**, *14*, 1704443.
- (85) Yuan, H.; Zhao, Y.; Duan, J.; Wang, Y.; Yang, X.; Tang, Q. All-Inorganic CsPbBr<sub>3</sub> Perovskite Solar Cell with 10.26% Efficiency by Spectra Engineering. *J. Mater. Chem. A* **2018**, *6*, 24324–24329.
- (86) Duan, J.; Zhao, Y.; He, B.; Tang, Q. High-Purity Inorganic Perovskite Films for Solar Cells with 9.72% Efficiency. *Angew. Chem.* **2018**, *130*, 3849–3853.
- (87) Abib, M. H.; Li, J.; Yang, H.; Wang, M.; Chen, T.; EnzeXu; Jiang, Y. Direct Deposition of Sn-Doped CsPbBr<sub>3</sub> Perovskite for Efficient Solar Cell Application. *RSC Adv.* **2021**, *11*, 3380–3389.
- (88) Duan, J.; Dou, D.; Zhao, Y.; Wang, Y.; Yang, X.; Yuan, H.; He, B.; Tang, Q. Spray-Assisted Deposition of CsPbBr<sub>3</sub> Films in Ambient Air for Large-Area Inorganic Perovskite Solar Cells. *Mater. Today Energy* **2018**, *10*, 146–152.
- (89) Zhang, W.; Liu, X.; He, B.; Zhu, J.; Li, X.; Shen, K.; Chen, H.; Duan, Y.; Tang, Q. Enhanced Efficiency of Air-Stable CsPbBr<sub>3</sub> Perovskite Solar Cells by Defect Dual Passivation and Grain Size Enlargement with a Multifunctional Additive. *ACS Appl. Mater. Interfaces* **2020**, *12*, 36092–36101.
- (90) Han, X.; Feng, J.; Zhu, Z.; Bao, C.; Huang, H.; Yu, T.; Feng, S.; Wang, X.; Li, Z.; Zou, Z. An Energy Level Alignment Strategy to Boost the Open-Circuit Voltage via a Mg:TiO<sub>2</sub> Compact Layer in the Planar Heterojunction CsPbBr<sub>3</sub> Solar Cells. *Appl. Phys. Lett.* **2022**, *120*, 201601.
- (91) Cao, X.; Zhang, G.; Cai, Y.; Jiang, L.; Chen, Y.; He, X.; Zeng, Q.; Jia, Y.; Xing, G.; Wei, J. Enhanced Performance of CsPbBr<sub>3</sub> Perovskite Solar Cells by Reducing the Conduction Band Offsets via a Sr-Modified TiO<sub>2</sub> Layer. *Appl. Surf. Sci.* **2020**, *529*, No. 147119.
- (92) Zhou, S.; Tang, R.; Yin, L. Slow-Photon-Effect-Induced Photoelectrical-Conversion Efficiency Enhancement for Carbon-Quantum-Dot-Sensitized Inorganic CsPbBr<sub>3</sub> Inverse Opal Perovskite Solar Cells. *Adv. Mater.* **2017**, *29*, 1703682.
- (93) Xu, H.; Duan, J.; Zhao, Y.; Jiao, Z.; He, B.; Tang, Q. 9.13%-Efficiency and Stable Inorganic CsPbBr<sub>3</sub> Solar Cells. Lead-Free CsSnBr<sub>3-x</sub>I<sub>x</sub> Quantum Dots Promote Charge Extraction. *J. Power Sources* **2018**, *399*, 76–82.
- (94) Mehrabian, M.; Afshar, E. N.; Yousefzadeh, S. A. Simulating the Thickness Effect of the Graphene Oxide Layer in CsPbBr<sub>3</sub>-Based Solar Cells. *Mater. Res. Express* **2021**, *8*, No. 035509.
- (95) Ullah, S.; Liu, P.; Wang, J.; Yang, P.; Liu, L.; Yang, S.-E.; Guo, H.; Xia, T.; Chen, Y. Optimizing the Working Mechanism of the CsPbBr<sub>3</sub>-Based Inorganic Perovskite Solar Cells for Enhanced Efficiency. *Sol. Energy* **2020**, *209*, 79–84.
- (96) Mehrabian, M.; Dalir, S.; Mahmoudi, G.; Miroslaw, B.; Babashkina, M. G.; Dektereva, A. V.; Safin, D. A. A Highly Stable All-Inorganic CsPbBr<sub>3</sub> Perovskite Solar Cell. *Eur. J. Inorg. Chem.* **2019**, *2019*, 3699–3703.